Analysis of first LIGO science data for stochastic gravitational waves

B. Abbott,[13] R. Abbott,[16] R. Adhikari,[14] A. Ageev,[21,28] B. Allen,[40] R. Amin,[35] S. B. Anderson,[13] W. G. Anderson,[30] M. Araya,[13] H. Armandula,[13] F. Asiri,[13,a] P. Aufmuth,[32] C. Aulbert,[1] S. Babak,[7] R. Balasubramanian,[7] S. Ballmer,[14] B. C. Barish,[13] D. Barker,[15] C. Barker-Patton,[15] M. Barnes,[13] B. Barr,[36] M. A. Barton,[13] K. Bayer,[14] R. Beausoleil,[27,b] K. Belczynski,[24] R. Bennett,[36,c] S. J. Berukoff,[1,d] J. Betzwieser,[14] B. Bhawal,[13] I. A. Bilenko,[21] G. Billingsley,[13] E. Black,[13] K. Blackburn,[13] B. Bland-Weaver,[15] B. Bochner,[14,e] L. Bogue,[13] R. Bork,[13] S. Bose,[41] P. R. Brady,[40] V. B. Braginsky,[21] J. E. Brau,[38] D. A. Brown,[40] S. Brozek,[32,f] A. Bullington,[27] A. Buonanno,[6,g] R. Burgess,[14] D. Busby,[13] W. E. Butler,[39] R. L. Byer,[27] L. Cadonati,[14] G. Cagnoli,[36] J. B. Camp,[22] C. A. Cantley,[36] L. Cardenas,[13] K. Carter,[16] M. M. Casey,[36] J. Castiglione,[35] A. Chandler,[13] J. Chapsky,[13,h] P. Charlton,[13] S. Chatterji,[14] Y. Chen,[6] V. Chickarmane,[17] D. Chin,[37] N. Christensen,[8] D. Churches,[7] C. Colacino,[32,2] R. Coldwell,[35] M. Coles,[16,i] D. Cook,[15] T. Corbitt,[14] D. Coyne,[13] J. D. E. Creighton,[40] T. D. Creighton,[13] D. R. M. Crooks,[36] P. Csatorday,[14] B. J. Cusack,[3] C. Cutler,[1] E. D'Ambrosio,[13] K. Danzmann,[32,2,20] R. Davies,[7] E. Daw,[17,j] D. DeBra,[27] T. Delker,[35,k] R. DeSalvo,[13] S. Dhurandhar,[12] M. Díaz,[30] H. Ding,[13] R. W. P. Drever,[4] R. J. Dupuis,[36] C. Ebeling,[8] J. Edlund,[13] P. Ehrens,[13] E. J. Elliffe,[36] T. Etzel,[13] M. Evans,[13] T. Evans,[16] C. Fallnich,[32] D. Farnham,[13] M. M. Fejer,[27] M. Fine,[13] L. S. Finn,[29] É. Flanagan,[9] A. Freise,[2,l] R. Frey,[38] P. Fritschel,[14] V. Frolov,[16] M. Fyffe,[16] K. S. Ganezer,[5] J. A. Giaime,[17] A. Gillespie,[13,m] K. Goda,[14] G. González,[17] S. Goßler,[32] P. Grandclément,[24] A. Grant,[36] C. Gray,[15] A. M. Gretarsson,[16] D. Grimmett,[13] H. Grote,[2] S. Grunewald,[1] M. Guenther,[15] E. Gustafson,[27,n] R. Gustafson,[37] W. O. Hamilton,[17] M. Hammond,[16] J. Hanson,[16] C. Hardham,[27] G. Harry,[14] A. Hartunian,[13] J. Heefner,[13] Y. Hefetz,[14] G. Heinzel,[2] I. S. Heng,[32] M. Hennessy,[27] N. Hepler,[29] A. Heptonstall,[36] M. Heurs,[32] M. Hewitson,[36] N. Hindman,[15] P. Hoang,[13] J. Hough,[36] M. Hrynevych,[13,o] W. Hua,[27] R. Ingley,[34] M. Ito,[38] Y. Itoh,[1] A. Ivanov,[13] O. Jennrich,[36,p] W. W. Johnson,[17] W. Johnston,[30] L. Jones,[13] D. Jungwirth,[13,q] V. Kalogera,[24] E. Katsavounidis,[14] K. Kawabe,[20,2] S. Kawamura,[23] W. Kells,[13] J. Kern,[16] A. Khan,[16] S. Killbourn,[36] C. J. Killow,[36] C. Kim,[24] C. King,[13] P. King,[13] S. Klimenko,[35] P. Kloevekorn,[2] S. Koranda,[40] K. Kötter,[32] J. Kovalik,[16] D. Kozak,[13] B. Krishnan,[1] M. Landry,[15] J. Langdale,[16] B. Lantz,[27] R. Lawrence,[14] A. Lazzarini,[13] M. Lei,[13] V. Leonhardt,[32] I. Leonor,[38] K. Libbrecht,[13] P. Lindquist,[13] S. Liu,[13] J. Logan,[13,r] M. Lormand,[16] M. Lubinski,[15] H. Lück,[32,2] T. T. Lyons,[13,r] B. Machenschalk,[1] M. MacInnis,[14] M. Mageswaran,[13] K. Mailand,[13] W. Majid,[13,h] M. Malec,[32] F. Mann,[13] A. Marin,[14,s] S. Márka,[13] E. Maros,[13] J. Mason,[13,t] K. Mason,[14] O. Matherny,[15] L. Matone,[15] N. Mavalvala,[14] R. McCarthy,[15] D. E. McClelland,[3] M. McHugh,[19] P. McNamara,[36,u] G. Mendell,[15] S. Meshkov,[13] C. Messenger,[34] V. P. Mitrofanov,[21] G. Mitselmakher,[35] R. Mittleman,[14] O. Miyakawa,[13] S. Miyoki,[13,v] S. Mohanty,[1,w] G. Moreno,[15] K. Mossavi,[2] B. Mours,[13,x] G. Mueller,[35] S. Mukherjee,[1,w] J. Myers,[15] S. Nagano,[2] T. Nash,[10,y] H. Naundorf,[1] R. Nayak,[12] G. Newton,[36] F. Nocera,[13] P. Nutzman,[24] T. Olson,[25] B. O'Reilly,[16] D. J. Ottaway,[14] A. Ottewill,[40,z] D. Ouimette,[13,q] H. Overmier,[16] B. J. Owen,[29] M. A. Papa,[1] C. Parameswariah,[16] V. Parameswariah,[15] M. Pedraza,[13] S. Penn,[11] M. Pitkin,[36] M. Plissi,[36] M. Pratt,[14] V. Quetschke,[32] F. Raab,[15] H. Radkins,[15] R. Rahkola,[38] M. Rakhmanov,[35] S. R. Rao,[13] D. Redding,[13,h] M. W. Regehr,[13,h] T. Regimbau,[14] K. T. Reilly,[13] K. Reithmaier,[13] D. H. Reitze,[35] S. Richman,[14,aa] R. Riesen,[16] K. Riles,[37] A. Rizzi,[16,bb] D. I. Robertson,[36] N. A. Robertson,[36,27] L. Robison,[13] S. Roddy,[16] J. Rollins,[14] J. D. Romano,[30,cc] J. Romie,[13] H. Rong,[35,m] D. Rose,[13] E. Rotthoff,[29] S. Rowan,[36] A. Rüdiger,[20,2] P. Russell,[13] K. Ryan,[15] I. Salzman,[13] G. H. Sanders,[13] V. Sannibale,[13] B. Sathyaprakash,[7] P. R. Saulson,[28] R. Savage,[15] A. Sazonov,[35] R. Schilling,[20,2] K. Schlaufman,[29] V. Schmidt,[13,dd] R. Schofield,[38] M. Schrempel,[32,ee] B. F. Schutz,[1,7] P. Schwinberg,[15] S. M. Scott,[3] A. C. Searle,[3] B. Sears,[13] S. Seel,[13] A. S. Sengupta,[12] C. A. Shapiro,[29,ff] P. Shawhan,[13] D. H. Shoemaker,[14] Q. Z. Shu,[35,gg] A. Sibley,[16] X. Siemens,[40] L. Sievers,[13,h] D. Sigg,[15] A. M. Sintes,[1,33] K. Skeldon,[36] J. R. Smith,[2] M. Smith,[14] M. R. Smith,[13] P. Sneddon,[36] R. Spero,[13,h] G. Stapfer,[16] K. A. Strain,[36] D. Strom,[38] A. Stuver,[29] T. Summerscales,[29] M. C. Sumner,[13] P. J. Sutton,[29,y] J. Sylvestre,[13] A. Takamori,[13] D. B. Tanner,[35] H. Tariq,[13] I. Taylor,[7] R. Taylor,[13] K. S. Thorne,[6] M. Tibbits,[29] S. Tilav,[13,hh] M. Tinto,[4,h] K. V. Tokmakov,[21] C. Torres,[30] C. Torrie,[13,36] S. Traeger,[32,ii] G. Traylor,[16] W. Tyler,[13] D. Ugolini,[31] M. Vallisneri,[6,jj] M. van Putten,[14] S. Vass,[13] A. Vecchio,[34] C. Vorvick,[15] S. P. Vyachanin,[21] L. Wallace,[13] H. Walther,[20] H. Ward,[36] B. Ware,[13,h] K. Watts,[16] D. Webber,[13] A. Weidner,[20,2] U. Weiland,[32] A. Weinstein,[13] R. Weiss,[14] H. Welling,[32] L. Wen,[13] S. Wen,[17] J. T. Whelan,[19] S. E. Whitcomb,[13] B. F. Whiting,[35] P. A. Willems,[13] P. R. Williams,[1,kk] R. Williams,[4] B. Willke,[32,2] A. Wilson,[13] B. J. Winjum,[29,d] W. Winkler,[20,2] S. Wise,[35] A. G. Wiseman,[40] G. Woan,[36] R. Wooley,[16] J. Worden,[15] I. Yakushin,[16] H. Yamamoto,[13] S. Yoshida,[26] I. Zawischa,[32,ll] L. Zhang,[13] N. Zotov,[18] M. Zucker,[16] and J. Zweizig[13]

(LIGO Scientific Collaboration)[mm]

[1]*Albert-Einstein-Institut, Max-Planck-Institut für Gravitationsphysik, D-14476 Golm, Germany*

[2]*Albert-Einstein-Institut, Max-Planck-Institut für Gravitationsphysik, D-30167 Hannover, Germany*

[3]*Australian National University, Canberra, 0200, Australia*

[4]*California Institute of Technology, Pasadena, California 91125, USA*

[5]*California State University Dominguez Hills, Carson, California 90747, USA*

[6]*Caltech-CaRT, Pasadena, California 91125, USA*

[7]*Cardiff University, Cardiff, CF2 3YB, United Kingdom*

[8]*Carleton College, Northfield, Minnesota 55057, USA*

[9]*Cornell University, Ithaca, New York 14853, USA*

[10]*Fermi National Accelerator Laboratory, Batavia, Illinois 60510, USA*

[11]*Hobart and William Smith Colleges, Geneva, New York 14456, USA*
[12]*Inter-University Centre for Astronomy and Astrophysics, Pune 411007, India*
[13]*LIGO–California Institute of Technology, Pasadena, California 91125, USA*
[14]*LIGO–Massachusetts Institute of Technology, Cambridge, Massachusetts 02139, USA*
[15]*LIGO Hanford Observatory, Richland, Washington 99352, USA*
[16]*LIGO Livingston Observatory, Livingston, Louisiana 70754, USA*
[17]*Louisiana State University, Baton Rouge, Louisiana 70803, USA*
[18]*Louisiana Tech University, Ruston, Louisiana 71272, USA*
[19]*Loyola University, New Orleans, Louisiana 70118, USA*
[20]*Max Planck Institut für Quantenoptik, D-85748, Garching, Germany*
[21]*Moscow State University, Moscow, 119992, Russia*
[22]*NASA/Goddard Space Flight Center, Greenbelt, Maryland 20771, USA*
[23]*National Astronomical Observatory of Japan, Tokyo 181-8588, Japan*
[24]*Northwestern University, Evanston, Illinois 60208, USA*
[25]*Salish Kootenai College, Pablo, Montana 59855, USA*
[26]*Southeastern Louisiana University, Hammond, Louisiana 70402, USA*
[27]*Stanford University, Stanford, California 94305, USA*
[28]*Syracuse University, Syracuse, New York 13244, USA*
[29]*The Pennsylvania State University, University Park, Pennsylvania 16802, USA*
[30]*The University of Texas at Brownsville and Texas Southmost College, Brownsville, Texas 78520, USA*
[31]*Trinity University, San Antonio, Texas 78212, USA*
[32]*Universität Hannover, D-30167 Hannover, Germany*
[33]*Universitat de les Illes Balears, E-07071 Palma de Mallorca, Spain*
[34]*University of Birmingham, Birmingham, B15 2TT, United Kingdom*
[35]*University of Florida, Gainsville, Florida 32611, USA*
[36]*University of Glasgow, Glasgow, G12 8QQ, United Kingdom*
[37]*University of Michigan, Ann Arbor, Michigan 48109, USA*
[38]*University of Oregon, Eugene, Oregon 97403, USA*
[39]*University of Rochester, Rochester, New York 14627, USA*
[40]*University of Wisconsin–Milwaukee, Milwaukee, Wisconsin 53201, USA*
[41]*Washington State University, Pullman, Washington 99164, USA*
(Received 14 January 2004; published 30 June 2004)

We present the analysis of between 50 and 100 h of coincident interferometric strain data used to search for and establish an upper limit on a stochastic background of gravitational radiation. These data come from the first LIGO science run, during which all three LIGO interferometers were operated over a 2-week period spanning August and September of 2002. The method of cross correlating the outputs of two interferometers is used for analysis. We describe in detail practical signal processing issues that arise when working with real data, and we establish an observational upper limit on a f^{-3} power spectrum of gravitational waves. Our 90% confidence limit is $\Omega_0 h_{100}^2 \leqslant 23 \pm 4.6$ in the frequency band 40–314 Hz, where h_{100} is the Hubble constant in units of 100 km/sec/Mpc and Ω_0 is the gravitational wave energy density per logarithmic frequency interval in units of the closure density. This limit is approximately 10^4 times better than the previous, broadband direct limit using interferometric detectors, and nearly 3 times better than the best narrow-band bar detector limit. As LIGO and other worldwide detectors improve in sensitivity and attain their design goals, the analysis procedures described here should lead to stochastic background sensitivity levels of astrophysical interest.

DOI: 10.1103/PhysRevD.69.122004 PACS number(s): 04.80.Nn, 04.30.Db, 07.05.Kf, 95.55.Ym

I. INTRODUCTION

In the last few years a number of new gravitational wave detectors, using long-baseline laser interferometry, have begun operation. These include the Laser Interferometer Gravitational Wave Observatory (LIGO) detectors located in Hanford, WA and Livingston, LA [1]; the GEO-600 detector near Hannover, Germany [2]; the VIRGO detector near Pisa, Italy [3]; and the Japanese TAMA-300 detector in Tokyo [4]. While all of these instruments are still being commissioned to perform at their designed sensitivity levels, many have begun making dedicated data collecting runs and performing gravitational wave search analyses on these data.

[a]Currently at Stanford Linear Accelerator Center.
[b]Permanent Address: HP Laboratories.
[c]Currently at Rutherford Appleton Laboratory.

In particular, from 23 August 2002 to 9 September 2002, the LIGO Hanford and LIGO Livingston Observatories (LHO and LLO) collected coincident science data; this first scientific data run is referred to as S1. The LHO site contains two identically oriented interferometers: one having 4-km-long measurement arms (referred to as H1), and one having 2-km-long arms (H2); the LLO site contains a single, 4-km-long interferometer (L1). GEO-600 also took data in coincidence with the LIGO detectors during that time. Members of the LIGO Scientific Collaboration have been analyzing these data to search for gravitational wave signals. These initial analyses are aimed at developing the search techniques and machinery, and at using these fundamentally new instruments to tighten upper limits on gravitational wave sources. Here we report on the methods and results of an analysis performed on the LIGO data to set an upper limit on a stochastic background of gravitational waves.[1] This represents the first such analysis performed on data from these new long-baseline detectors. The outline of the paper is as follows:

Section II gives a description of the LIGO instruments and a summary of their operational characteristics during the S1 data run. In Sec. III, we give a brief description of the properties of a stochastic background of gravitational radiation, and Sec. IV reviews the basic analysis method of cross correlating the outputs of two gravitational wave detectors.

In Sec. V, we discuss in detail the analysis performed on the LIGO data set. In applying the basic cross-correlation technique to real detector data, we have addressed some practical issues and performed some additional analyses that have not been dealt with previously in the literature: (i) avoidance of spectral leakage in the short-time Fourier transforms of the data; (ii) a procedure for identifying and removing narrow-band (discrete frequency) correlations between detectors; (iii) chi-squared and time shift analyses, designed to explore the frequency domain character of the cross correlations.

In Sec. VI, the error estimation is presented, and in Sec. VII, we show how the procedure has been tested by analyzing data that contain an artificially injected, simulated stochastic background signal. Section VIII discusses in more detail the instrumental correlation that is observed between the two Hanford interferometers (H1 and H2), and Sec. IX concludes the paper with a brief summary and topics for future work.

The appendix gives a list of symbols used in the paper, along with their descriptions and equation numbers or sections in which they were defined.

II. LIGO DETECTORS

An interferometric gravitational-wave detector attempts to measure oscillations in the space-time metric, utilizing the apparent change in light travel time induced by a gravitational wave. At the core of each LIGO detector is an orthogonal arm Michelson laser interferometer, as its geometry is well-matched to the space-time distortion. During any half-cycle of the oscillation, the quadrupolar gravitational-wave field increases the light travel time in one arm and decreases it in the other arm. Since the gravitational wave produces the equivalent of a strain in space, the travel time change is proportional to the arm length, hence the long arms. Each arm contains two test masses, a partially transmitting mirror near the beam splitter and a near-perfect reflector at the end of the arm. Each such pair is oriented to form a resonant Fabry-Perot cavity, which further increases the strain induced phase shifts by a factor proportional to the cavity finesse. An additional partially transmitting mirror is placed in the input path to form the power-recycling cavity, which increases the power incident on the beam splitter, thereby decreasing the shot-noise contribution to the signal-to-noise ratio of the gravitational-wave signal.

[1]Given the GEO S1 sensitivity level and large geographical separation of the GEO-600 and LIGO detectors, it was not profitable to include GEO-600 data in this analysis.

[d]Currently at University of California, Los Angeles.
[e]Currently at Hofstra University.
[f]Currently at Siemens AG.
[g]Permanent address: GReCO, Institut d'Astrophysique de Paris (CNRS).
[h]Currently at NASA Jet Propulsion Laboratory.
[i]Currently at National Science Foundation.
[j]Currently at University of Sheffield.
[k]Currently at Ball Aerospace Corporation.
[l]Currently at European Gravitational Observatory.
[m]Currently at Intel Corp.
[n]Currently at Lightconnect Inc.
[o]Currently at Keck Observatory.
[p]Currently at ESA Science and Technology Center.
[q]Currently at Raytheon Corporation.
[r]Currently at Mission Research Corporation.
[s]Currently at Harvard University.
[t]Currently at Lockheed-Martin Corporation.
[u]Currently at NASA Goddard Space Flight Center.
[v]Permanent address: University of Tokyo, Institute for Cosmic Ray Research.
[w]Currently at The University of Texas at Brownsville and Texas Southmost College.
[x]Currently at Laboratoire d'Annecy-le-Vieux de Physique des Particules.
[y]Currently at LIGO–California Institute of Technology.
[z]Permanent address: University College Dublin.
[aa]Currently at Research Electro-Optics Inc.
[bb]Currently at Institute of Advanced Physics, Baton Rouge, LA.
[cc]Currently at Cardiff University.
[dd]Currently at European Commission, DG Research, Brussels, Belgium.
[ee]Currently at Spectra Physics Corporation.
[ff]Currently at University of Chicago.
[gg]Currently at LightBit Corporation.
[hh]Currently at University of Delaware.
[ii]Currently at Carl Zeiss GmbH.
[jj]Permanent address: NASA Jet Propulsion Laboratory.
[kk]Currently at Shanghai Astronomical Observatory.
[ll]Currently at Laser Zentrum Hannover.
[mm]http://www.ligo.org

Each interferometer is illuminated with a medium power Nd:YAG laser, operating at 1.06 microns [5]. Before the light is launched into the interferometer, its frequency, amplitude and direction are all stabilized, using a combination of active and passive stabilization techniques. To isolate the test masses and other optical elements from ground and acoustic vibrations, the detectors implement a combination of passive and active seismic isolation systems [6,7], from which the mirrors are suspended as pendulums. This forms a coupled oscillator system with high isolation for frequencies above 40 Hz. The test masses, major optical components, vibration isolation systems, and main optical paths are all enclosed in a high vacuum system.

Various feedback control systems are used to keep the multiple optical cavities tightly on resonance [8] and well aligned [9]. The gravitational wave strain signal is obtained from the error signal of the feedback loop used to control the differential motion of the interferometer arms. To calibrate the error signal, the effect of the feedback loop gain is measured and divided out, and the response $\tilde{R}(f)$ to a differential arm strain is measured and factored in. For the latter, the absolute scale is established using the laser wavelength, and measuring the mirror drive signal required to move through a given number of interference fringes. During interferometer operation, the calibration was tracked by injecting fixed-amplitude sinusoidal signals into the differential arm control loop, and monitoring the amplitude of these signals at the measurement (error) point [10].

Figure 1 shows reference amplitude spectra of equivalent strain noise, for the three LIGO interferometers during the S1 run. The eventual strain noise goal is also indicated for comparison. The differences among the three spectra reflect differences in the operating parameters and hardware implementations of the three instruments; they are in various stages of reaching the final design configuration. For example, all interferometers operated during S1 at a substantially lower effective laser power level than the eventual level of 6 W at the interferometer input; the resulting reduction in signal-to-noise ratio is even greater than the square root of the power reduction, because the detection scheme is designed to be efficient only near the design power level. Thus the shot-noise region of the spectrum (above 200 Hz) is much higher than the design goal. Other major differences between the S1 state and the final configuration were: partially implemented laser frequency and amplitude stabilization systems; and partially implemented alignment control systems.

Two other important characteristics of the instruments' performance are the stationarity of the noise, and the duty cycle of operation. The noise was significantly nonstationary, due to the partial stabilization and controls mentioned above. In the frequency band of most importance to this analysis, approximately 60–300 Hz, a factor of 2 variation in the noise amplitude over several hours was typical for the instruments; this is addressed quantitatively in Sec. VI and Fig. 10. As our analysis relies on cross correlating the outputs of two detectors, the relevant duty cycle measures are those for double-coincident operation. For the S1 run, the total times of coincident science data for the three pairs are: H1-H2, 188 h (46% duty cycle over the S1 duration); H1-L1, 116 h (28%); H2-L1, 131 h (32%). A more detailed description of the LIGO interferometers and their performance during the S1 run can be found in Ref. [11].

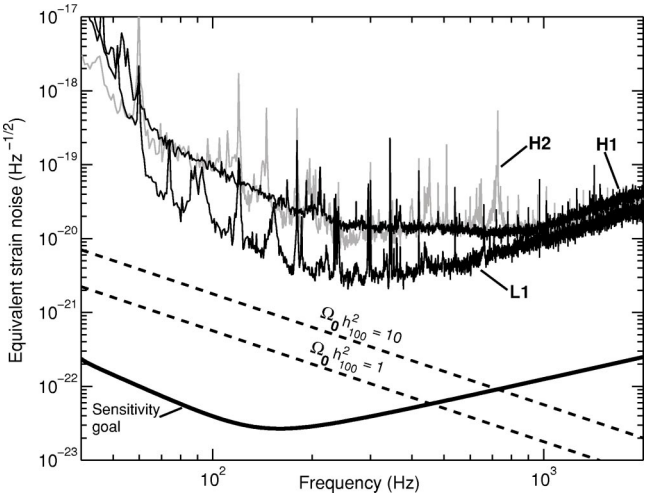

FIG. 1. Reference sensitivity curves for the three LIGO interferometers during the S1 data run, in terms of equivalent strain noise density. The H1 and H2 spectra are from 9 September 2002, and the L1 spectrum is from 7 September 2002. Also shown are strain spectra corresponding to two levels of a stochastic background of gravitational radiation defined by Eq. (3.7). These can be compared to the expected 90% confidence level upper limits, assuming Gaussian uncorrelated detector noise at the levels shown here, for the interferometer pairs: H2-L1 ($\Omega_0 h^2_{100}=10$), with 100 h of correlated integration time; H1-H2 ($\Omega_0 h^2_{100}=0.83$), with 150 h of integration time; and H1-L1 ($\Omega_0 h^2_{100}=11$), with 100 h of integration time. Also shown is the strain noise goal for the two 4-km arm interferometers (H1 and L1).

III. STOCHASTIC GRAVITATIONAL WAVE BACKGROUNDS

A. Spectrum

A stochastic background of gravitational radiation is analogous to the cosmic microwave background radiation, though its spectrum is unlikely to be thermal. Sources of a stochastic background could be cosmological or astrophysical in origin. Examples of the former are zero-point fluctuations of the space-time metric amplified during inflation, and first-order phase transitions and decaying cosmic string networks in the early universe. An example of an astrophysical source is the random superposition of many weak signals from binary-star systems. See Refs. [12] and [13] for a review of sources.

The spectrum of a stochastic background is usually described by the dimensionless quantity $\Omega_{\rm gw}(f)$ which is the gravitational-wave energy density per unit logarithmic frequency, divided by the critical energy density ρ_c to close the universe:

$$\Omega_{\rm gw}(f) \equiv \frac{f}{\rho_c}\frac{d\rho_{\rm gw}}{df}. \tag{3.1}$$

The critical density $\rho_c \equiv 3c^2 H_0^2/8\pi G$ depends on the present day Hubble expansion rate H_0. For convenience we define a dimensionless factor

$$h_{100} \equiv H_0 / H_{100}, \tag{3.2}$$

where

$$H_{100} \equiv 100 \frac{\text{km}}{\text{sec} \cdot \text{Mpc}} \approx 3.24 \times 10^{-18} \frac{1}{\text{sec}}, \tag{3.3}$$

to account for the different values of H_0 that are quoted in the literature.[2] Note that $\Omega_{\text{gw}}(f) h_{100}^2$ is independent of the actual Hubble expansion rate, so we work with this quantity rather than $\Omega_{\text{gw}}(f)$ alone.

Our specific interest is the measurable one-sided power spectrum of the gravitational wave strain $S_{\text{gw}}(f)$, which is normalized according to:

$$\lim_{T \to \infty} \frac{1}{T} \int_{-T/2}^{T/2} dt |h(t)|^2 = \int_0^\infty df S_{\text{gw}}(f), \tag{3.4}$$

where $h(t)$ is the strain in a single detector due to the gravitational wave signal; $h(t)$ can be expressed in terms of the perturbations h_{ab} of the spacetime metric and the detector geometry via:

$$h(t) \equiv h_{ab}(t, \vec{x}_0) \frac{1}{2} (\hat{X}^a \hat{X}^b - \hat{Y}^a \hat{Y}^b). \tag{3.5}$$

Here $\vec{x}_0$ specifies the coordinates of the interferometer vertex, and $\hat{X}^a, \hat{Y}^a$ are unit vectors pointing in the direction of the detector arms. Since the energy density in gravitational waves involves a product of time derivatives of the metric perturbations (cf. p. 955 of Ref. [17]), one can show (see, e.g., Secs. II A and III A in Ref. [18] for more details) that $S_{\text{gw}}(f)$ is related to $\Omega_{\text{gw}}(f)$ via:

$$S_{\text{gw}}(f) = \frac{3H_0^2}{10\pi^2} f^{-3} \Omega_{\text{gw}}(f). \tag{3.6}$$

Thus, for a stochastic gravitational wave background with $\Omega_{\text{gw}}(f) \equiv \Omega_0 = \text{const}$ (as is predicted at LIGO frequencies e.g., by inflationary models in the infinitely slow-roll limit, or by cosmic string models [19]) the power in gravitational waves falls off as $1/f^3$, with a strain amplitude scale of:

$$S_{\text{gw}}^{1/2}(f) = 5.6 \times 10^{-22} h_{100} \sqrt{\Omega_0} \left(\frac{100 \text{ Hz}}{f} \right)^{3/2} \text{Hz}^{-1/2}. \tag{3.7}$$

The spectrum $\Omega_{\text{gw}}(f)$ completely specifies the statistical properties of a stochastic background of gravitational radiation provided we make several additional assumptions. Here, we assume that the stochastic background is isotropic, unpolarized, stationary, and Gaussian. Anisotropic or non-Gaussian backgrounds (e.g., due to an incoherent superposition of gravitational waves from a large number of unresolved white dwarf binary star systems in our own galaxy, or a ''popcorn'' stochastic signal produced by gravitational waves from supernova core-collapse events [20,21]) may require different data analysis techniques from those presented here. (See, e.g., Refs. [22,23] for discussions of these different techniques.)

B. Prior observational constraints

While predictions for $\Omega_{\text{gw}}(f)$ from cosmological models can vary over many orders of magnitude, there are several observational results that place interesting upper limits on $\Omega_{\text{gw}}(f)$ in various frequency bands. Table I summarizes these observational constraints and upper limits on the energy density of a stochastic gravitational wave background. The high degree of isotropy observed in the cosmic microwave background radiation (CMBR) places a strong constraint on $\Omega_{\text{gw}}(f)$ at very low frequencies [24]. Since $H_{100} \approx 3.24 \times 10^{-18}$ Hz, this limit applies only over several decades of frequency $10^{-18} - 10^{-16}$ Hz which are far below the bands accessible to investigation by either Earth-based (10–10^4 Hz) or space-based (10^{-4}–10^{-1} Hz) detectors.

Another observational constraint comes from nearly two decades of monitoring the time-of-arrival jitter of radio pulses from a number of millisecond pulsars [25]. These pulsars are remarkably stable clocks, and the regularity of their pulses places tight constraints on $\Omega_{\text{gw}}(f)$ at frequencies on the order of the inverse of the observation time of the pulsars, $1/T \sim 10^{-8}$ Hz. Like the constraint derived from the isotropy of the CMBR, the millisecond pulsar timing constraint applies to an observational frequency band much lower than that probed by Earth-based and space-based detectors.

The only constraint on $\Omega_{\text{gw}}(f)$ within the frequency band of Earth-based detectors comes from the observed abundances of the light elements in the universe, coupled with the standard model of big-bang nucleosynthesis [26]. For a narrow range of key cosmological parameters, this model is in remarkable agreement with the elemental observations. One of the constrained parameters is the expansion rate of the universe at the time of nucleosynthesis, thus constraining the energy density of the universe at that time. This in turn constrains the energy density in a cosmological background of gravitational radiation (noncosmological sources of a stochastic background, e.g., from a superposition of supernovae signals, are not of course constrained by these observations). The observational constraint is on the logarithmic integral over frequency of $\Omega_{\text{gw}}(f)$.

All the above constraints were indirectly inferred via electromagnetic observations. There are a few, much weaker constraints on $\Omega_{\text{gw}}(f)$ that have been set by observations with detectors directly sensitive to gravitational waves. The earliest such measurement was made with room-temperature bar detectors, using a split bar technique for wide bandwidth performance [27]. Later measurements include an upper

[2] $H_0 = 73 \pm 2 \pm 7$ km/sec/Mpc as shown in Ref. [14] and from independent SNIa observations from observatories on the ground [15]. The Wilkinson Microwave Anisotropy Probe 1st year (WMAP1) observation has $H_0 = 71^{+4}_{-3}$ km/sec/Mpc [16].

TABLE I. Summary of upper limits on $\Omega_0 h_{100}^2$ over a large range of frequency bands. The upper portion of the table lists indirect limits derived from astrophysical observations. The lower portion of the table lists limits obtained from prior direct gravitational wave measurement.

Observational technique	Observed limit	Frequency domain	Comments
Cosmic microwave background	$\Omega_{\rm gw}(f)h_{100}^2 \leqslant 10^{-13}\left(\frac{10^{-16}\ {\rm Hz}}{f}\right)^2$	$3\times10^{-18}<f<10^{-16}$ Hz	[24]
Radio pulsar timing	$\Omega_{\rm gw}(f)h_{100}^2 \leqslant 9.3\times10^{-8}$	$4\times10^{-9}<f<4\times10^{-8}$ Hz	95% C.L. bound, [25]
Big-bang nucleosynthesis	$\int_{f>10^{-8}\ {\rm Hz}} d\ln f\,\Omega_{\rm gw}(f)h_{100}^2 \leqslant 10^{-5}$	$f>10^{-8}$ Hz	95% C.L. bound, [26]
Interferometers	$\Omega_{\rm gw}(f)h_{100}^2 \leqslant 3\times10^5$	$100 \leqslant f \leqslant 1000$ Hz	Garching-Glasgow [28]
Room temperature			
Resonant bar (correlation)	$\Omega_{\rm gw}(f_0)h_{100}^2 \leqslant 3000$	$f_0 = 985 \pm 80$ Hz	Glasgow [27]
Cryogenic resonant bar (single)	$\Omega_{\rm gw}(f_0)h_{100}^2 \leqslant 300$	$f_0 = 907$ Hz	Explorer [29]
	$\Omega_{\rm gw}(f_0)h_{100}^2 \leqslant 5000$	$f_0 = 1875$ Hz	ALTAIR [30]
Cryogenic resonant bar (correlation)	$\Omega_{\rm gw}(f_0)h_{100}^2 \leqslant 60$	$f_0 = 907$ Hz	Explorer+Nautilus [31,32]

limit from a correlation between the Garching and Glasgow prototype interferometers [28], several upper limits from observations with a single cryogenic resonant bar detector [29,30], and most recently an upper limit from observations of two-detector correlations between the Explorer and Nautilus cryogenic resonant bar detectors [31,32]. Note that the cryogenic resonant bar observations are constrained to a very narrow bandwidth ($\Delta f \sim 1$Hz) around the resonant frequency of the bar.

IV. DETECTION VIA CROSS CORRELATION

We can express the equivalent strain output $s_i(t)$ of each of our detectors as:

$$s_i(t) \equiv h_i(t) + n_i(t), \tag{4.1}$$

where $h_i(t)$ is the strain signal in the ith detector due to a gravitational wave background, and $n_i(t)$ is the detector's equivalent strain noise. If we had only one detector, all we could do would be to put an upper limit on a stochastic background at the detector's strain noise level; e.g., using L1 we could put a limit of $\Omega_0 h_{100}^2 \sim 10^3$ in the band 100–200 Hz. To do much better, we *cross correlate* the outputs of two detectors, taking advantage of the fact that the sources of noise n_i in each detector will, in general, be independent [12,13,18,33–35]. We thus compute the general cross correlation:[3]

$$Y \equiv \int_{-T/2}^{T/2} dt_1 \int_{-T/2}^{T/2} dt_2 s_1(t_1) Q(t_1 - t_2) s_2(t_2), \tag{4.2}$$

where $Q(t_1 - t_2)$ is a (real) filter function, which we will choose to maximize the signal-to-noise ratio of Y. Since the optimal choice of $Q(t_1 - t_2)$ falls off rapidly for time delays $|t_1 - t_2|$ large compared to the light travel time d/c between the two detectors,[4] and since a typical observation time T will be much, much greater than d/c, we can change the limits on one of the integrations from $(-T/2, T/2)$ to $(-\infty, \infty)$, and subsequently obtain [18]:

$$Y \approx \int_{-\infty}^{\infty} df \int_{-\infty}^{\infty} df'\, \delta_T(f - f') \tilde{s}_1^*(f) \tilde{Q}(f') \tilde{s}_2(f'), \tag{4.3}$$

where

$$\delta_T(f) \equiv \int_{-T/2}^{T/2} dt e^{-i2\pi ft} = \frac{\sin(\pi f T)}{\pi f} \tag{4.4}$$

is a finite-time approximation to the Dirac delta function, and $\tilde{s}_i(f), \tilde{Q}(f)$ denote the Fourier transforms of $s_i(t), Q(t)$—i.e., $\tilde{a}(f) \equiv \int_{-\infty}^{\infty} dt e^{-i2\pi ft} a(t)$.

To find the optimal $\tilde{Q}(f)$, we assume that the intrinsic detector noise is: (i) stationary over a measurement time T; (ii) Gaussian; (iii) uncorrelated between different detectors; (iv) uncorrelated with the stochastic gravitational wave sig-

[3]The equations in this section are a summary of Sec. III from Ref. [18]. Readers interested in more details and/or derivations of the key equations should refer to Ref. [18] and references contained therein.

[4]The light travel time d/c between the Hanford and Livingston detectors is approximately 10 msec.

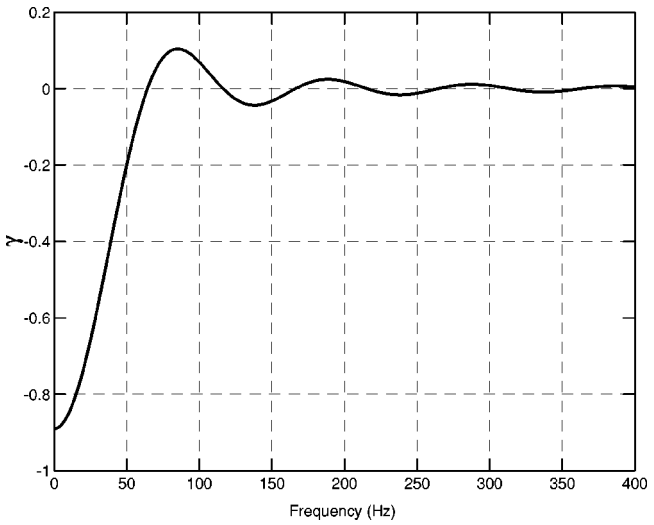

FIG. 2. Overlap reduction function between the LIGO Livingston and the LIGO Hanford sites. The value of $|\gamma|$ is a little less than unity at 0 Hz because the interferometer arms are not exactly co-planar and co-aligned between the two sites.

nal; and (v) much greater in power at any frequency than the stochastic gravitational wave background. Then the expected value of the cross correlation Y depends only on the stochastic signal:

$$\mu_Y \equiv \langle Y \rangle = \frac{T}{2}\int_{-\infty}^{\infty} df\, \gamma(|f|) S_{\rm gw}(|f|)\tilde{Q}(f), \tag{4.5}$$

while the variance of Y is dominated by the noise in the individual detectors:

$$\sigma_Y^2 \equiv \langle (Y-\langle Y\rangle)^2\rangle \approx \frac{T}{4}\int_{-\infty}^{\infty} df P_1(|f|)|\tilde{Q}(f)|^2 P_2(|f|). \tag{4.6}$$

Here $P_1(f)$ and $P_2(f)$ are the one-sided strain noise power spectra of the two detectors. The integrand of Eq. (4.5) contains a (real) function $\gamma(f)$, called the *overlap reduction function* [35], which characterizes the reduction in sensitivity to a stochastic background arising from the separation time delay and relative orientation of the two detectors. It is a function of only the relative detector geometry [for coincident and co-aligned detectors, like H1 and H2, $\gamma(f)=1$ for all frequencies]. A plot of the overlap reduction function for correlations between LIGO Livingston and LIGO Hanford is shown in Fig. 2.

From Eqs. (4.5) and (4.6), it is relatively straightforward to show [12] that the expected signal-to-noise ratio (μ_Y/σ_Y) of Y is maximized when

$$\tilde{Q}(f) \propto \frac{\gamma(|f|) S_{\rm gw}(|f|)}{P_1(|f|)P_2(|f|)}. \tag{4.7}$$

For the S1 analysis, we specialize to the case $\Omega_{\rm gw}(f) \equiv \Omega_0 = {\rm const}$. Then,

$$\tilde{Q}(f) = \mathcal{N}\frac{\gamma(|f|)}{|f|^3 P_1(|f|)P_2(|f|)}, \tag{4.8}$$

where $\mathcal{N}$ is a (real) overall normalization constant. In practice we choose $\mathcal{N}$ so that the expected cross correlation is $\mu_Y = \Omega_0 h_{100}^2 T$. For such a choice,

$$\mathcal{N} = \frac{20\pi^2}{3H_{100}^2}\left[\int_{-\infty}^{\infty} df \frac{\gamma^2(|f|)}{f^6 P_1(|f|)P_2(|f|)}\right]^{-1}, \tag{4.9}$$

$$\sigma_Y^2 \approx T\left(\frac{10\pi^2}{3H_{100}^2}\right)^2\left[\int_{-\infty}^{\infty} df \frac{\gamma^2(|f|)}{f^6 P_1(|f|)P_2(|f|)}\right]^{-1}. \tag{4.10}$$

In the sense that $\tilde{Q}(f)$ maximizes μ_Y/σ_Y, it is the *optimal filter* for the cross correlation Y. The signal-to-noise ratio $\rho_Y \equiv Y/\sigma_Y$ has expected value

$$\langle \rho_Y \rangle = \frac{\mu_Y}{\sigma_Y} \approx \frac{3H_0^2}{10\pi^2}\Omega_0\sqrt{T}\left[\int_{-\infty}^{\infty} df \frac{\gamma^2(|f|)}{f^6 P_1(|f|)P_2(|f|)}\right]^{1/2}, \tag{4.11}$$

which grows with the square-root of the observation time T, and inversely with the product of the *amplitude* noise spectral densities of the two detectors. In order of magnitude, Eq. (4.11) indicates that the upper limit we can place on $\Omega_0 h_{100}^2$ by cross correlation is smaller (i.e., more constraining) than that obtainable from one detector by a factor of $\gamma_{\rm rms}\sqrt{T\Delta_{\rm BW}}$, where $\Delta_{\rm BW}$ is the bandwidth over which the integrand of Eq. (4.11) is significant [roughly the width of the peak of $1/f^3 P_i(f)$], and $\gamma_{\rm rms}$ is the rms value of $\gamma(f)$ over that bandwidth. For the LHO-LLO correlations in this analysis, $T \sim 2\times 10^5$ sec, $\Delta_{\rm BW} \sim 100$ Hz, and $\gamma_{\rm rms} \sim 0.1$, so we expect to be able to set a limit that is a factor of several hundred below the individual detectors' strain noise,[5] or $\Omega_0 h_{100}^2 \sim 10$ as shown in Fig. 1.

V. ANALYSIS OF LIGO DATA

A. Data analysis pipeline

A flow diagram of the data analysis pipeline is shown in Fig. 3 [36]. We perform the analysis in the frequency domain, where it is more convenient to construct and apply the optimal filter. Since the data are discretely sampled, we use discrete Fourier transforms and sums over frequency bins rather than integrals. The data $r_i[k]$ are the raw (uncalibrated) detector outputs at discrete times $t_k \equiv k\,\delta t$:

$$r_i[k] \equiv r_i(t_k), \tag{5.1}$$

[5]More precisely, if the two detectors have unequal strain sensitivities, the cross-correlation limit will be a factor of $\gamma_{\rm rms}\sqrt{T\Delta_{\rm BW}}$ below the geometric mean of the two noise spectral densities.

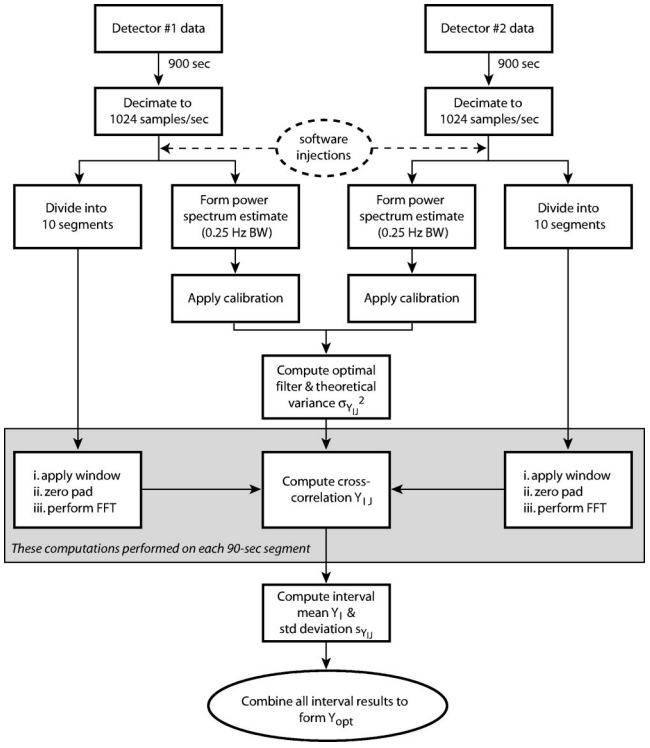

FIG. 3. Data analysis flow diagram for the stochastic search. The raw detector signal (i.e., the uncalibrated differential arm error signal) is fed into the pipeline in 900-sec-long intervals. Simulated stochastic background signals can be injected near the beginning of each data path, allowing us to test the data analysis routines in the presence of known correlations.

where $k=0,1,2,\ldots,$ δt is the sampling period, and i labels the detector. We decimate the data to a sampling rate of $(\delta t)^{-1}=1024$ Hz (from 16384 Hz), since the higher frequencies make a negligible contribution to the cross correlation. The decimation is performed with a finite impulse response filter of length 320, and cutoff frequency 512 Hz. The data are split into *intervals* (labeled by index I) and *segments* (labeled by index J) within each interval to deal with detector nonstationarity and to produce sets of cross-correlation values Y_{IJ} for which empirical variances can be calculated; see Fig. 4. The time-series data corresponding to the Jth segment in interval I is denoted $r_{iIJ}[k]$, where $k=0,1,\ldots,N-1$ runs over the total number of samples in the segment.

A single optimal filter $\tilde{Q}_I$ is calculated and applied for each interval I, the duration of which should be long enough to capture relatively narrow-band features in the power spectra, yet short enough to account for significant nonstationary detector noise. Based on observations of detector noise variation, we chose an interval duration of $T_{\rm int}=900$ sec. The segment duration should be much greater than the light travel time between the two detectors, yet short enough to yield a sufficient number of cross-correlation measurements within each interval to obtain an experimental estimate of the theoretical variance $\sigma_{Y_{IJ}}^2$ of the cross correlation statistic Y_{IJ}. We chose a segment duration of $T_{\rm seg}=90$ sec, yielding ten Y_{IJ} values per interval.

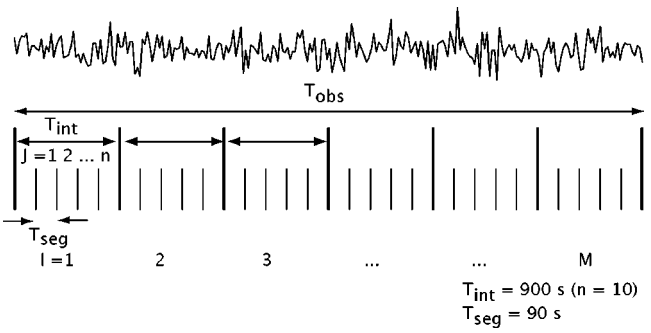

FIG. 4. Time-series data from each interferometer is split into M 900-sec intervals, which are further subdivided into $n=10$ 90-sec data segments. Cross-correlation values Y_{IJ} are calculated for each 90-sec segment; theoretical variances $\sigma_{Y_{IJ}}^2$ are calculated for each 900-sec interval. Here $I=1,2,\ldots,M$ labels the different intervals, and $J=1,2,\ldots,n$ labels the individual segments within each interval.

To compute the segment cross-correlation values Y_{IJ}, the raw decimated data $r_{iIJ}[k]$ are windowed in the time domain (see Sec. V B for details), zero padded to twice their length (to avoid wrap-around problems [37] when calculating the cross-correlation statistic in the frequency domain), and discrete Fourier transformed. Explicitly, defining

$$g_{iIJ}[k]\equiv\begin{cases} w_i[k]r_{iIJ}[k] & k=0,\ldots,N-1 \\ 0 & k=N,\ldots,2N-1, \end{cases} \tag{5.2}$$

where $w_i[k]$ is the window function for the ith detector,[6] the discrete Fourier transform is:

$$\tilde{g}_{iIJ}[q]\equiv\sum_{k=0}^{2N-1}\delta t g_{iIJ}[k]e^{-i2\pi kq/2N}, \tag{5.3}$$

where $N=T_{\rm seg}/\delta t=92160$ is the number of data points in a segment, and $q=0,1,\ldots,2N-1$. The cross spectrum $\tilde{g}_{1IJ}^*[q]\cdot\tilde{g}_{2IJ}[q]$ is formed and binned to the frequency resolution, δf, of the optimal filter $\tilde{Q}_I$:[7]

$$\mathcal{G}_{IJ}[\ell]\equiv\frac{1}{n_b}\sum_{q=n_b\ell-m}^{n_b\ell+m}\tilde{g}_{1IJ}^*[q]\tilde{g}_{2IJ}[q], \tag{5.4}$$

where $\ell_{\rm min}\leqslant\ell\leqslant\ell_{\rm max}$, $n_b=2T_{\rm seg}\delta f$ is the number of frequency values being binned, and $m=(n_b-1)/2$. The index ℓ labels the discrete frequencies, $f_\ell\equiv\ell\,\delta f$. The $\mathcal{G}_{IJ}[\ell]$ are computed for a range of ℓ that includes only the frequency band that yields most of the expected signal-to-noise ratio (e.g., 40–314 Hz for the LHO-LLO correlations), as described in Sec. V C. The cross-correlation values are calculated as:

$$Y_{IJ}\equiv 2\,\mathrm{Re}\left[\sum_{\ell=\ell_{\rm min}}^{\ell_{\rm max}}\delta f\tilde{Q}_I[\ell]\mathcal{G}_{IJ}[\ell]\right]. \tag{5.5}$$

[6]In general, one can use different window functions for different detectors. However, for the S1 analysis, we took $w_1[k]=w_2[k]$.

[7]As discussed below, $\delta f=0.25$ Hz yielding $n_b=45$ and $m=22$.

Some of the frequency bins within the $\{\ell_{\min},\ell_{\max}\}$ range are excluded from the above sum to avoid narrow-band instrumental correlations, as described in Sec. V C. Except for the details of windowing, binning, and band-limiting, Eq. (5.5) for Y_{IJ} is just a discrete-frequency approximation to Eq. (4.3) for Y for the continuous-frequency data, with $df'\,\delta_T(f-f')$ approximated by a Kronecker delta $\delta_{\ell\ell'}$ in discrete frequencies f_ℓ and $f_{\ell'}$.[8]

In calculating the optimal filter, we estimate the strain noise power spectra P_{iI} for the interval I using Welch's method: 449 periodograms are formed and averaged from 4096-point, Hann-windowed data segments, overlapped by 50%, giving a frequency resolution $\delta f = 0.25$ Hz. To calibrate the spectra in strain, we apply the calibration response function $\tilde{R}_i(f)$ which converts the raw data to equivalent strain: $\tilde{s}_i(f) = \tilde{R}_i^{-1}(f)\tilde{r}_i(f)$. The calibration lines described in Sec. II were measured once per 60 sec; for each interval I, we apply the response function, $\tilde{R}_{iI}$, corresponding to the middle 60 sec of the interval. The optimal filter $\tilde{Q}_I$ for the case $\Omega_{\rm gw}(f) \equiv \Omega_0 = \text{const}$ is then constructed as:

$$\tilde{Q}_I[\ell] \equiv \mathcal{N}_I \frac{\gamma[\ell]}{|f_\ell|^3 (\tilde{R}_{1I}[\ell]P_{1I}[\ell])^*(\tilde{R}_{2I}[\ell]P_{2I}[\ell])}, \quad (5.6)$$

where $\gamma[\ell] \equiv \gamma(f_\ell)$, and $\tilde{R}_{iI}[\ell] \equiv \tilde{R}_{iI}(f_\ell)$. By including the additional response function factors $\tilde{R}_{iI}$ in Eq. (5.6), $\tilde{Q}_I$ has the appropriate units to act directly on the raw detector outputs in the calculation of Y_{IJ} [cf. Eq. (5.5)].

The normalization factor $\mathcal{N}_I$ in Eq. (5.6) takes into account the effect of windowing [38]. Choosing $\mathcal{N}_I$ so that the theoretical mean of the cross correlation Y_{IJ} is equal to $\Omega_0 h_{100}^2 T_{\rm seg}$ for all I,J (as was done for Y in Sec. IV), we have:

$$\mathcal{N}_I = \frac{20\pi^2}{3H_{100}^2} \frac{1}{\overline{w_1 w_2}} \left[2 \sum_{\ell=\ell_{\min}}^{\ell_{\max}} \delta f \frac{\gamma^2[\ell]}{f_\ell^6 P_{1I}[\ell] P_{2I}[\ell]} \right]^{-1}, \quad (5.7)$$

$$\sigma_{Y_{IJ}}^2 = T_{\rm seg} \left(\frac{10\pi^2}{3H_{100}^2} \right)^2 \frac{\overline{w_1^2 w_2^2}}{(\overline{w_1 w_2})^2} \times \left[2 \sum_{\ell=\ell_{\min}}^{\ell_{\max}} \delta f \frac{\gamma^2[\ell]}{f_\ell^6 P_{1I}[\ell] P_{2I}[\ell]} \right]^{-1}, \quad (5.8)$$

where

$$\overline{w_1 w_2} \equiv \frac{1}{N} \sum_{k=0}^{N-1} w_1[k] w_2[k], \quad (5.9)$$

$$\overline{w_1^2 w_2^2} \equiv \frac{1}{N} \sum_{k=0}^{N-1} w_1^2[k] w_2^2[k], \quad (5.10)$$

provided the windowing is sufficient to prevent significant leakage of power across the frequency band (see Sec. V B and Ref. [38] for more details). Note that the theoretical variance $\sigma_{Y_{IJ}}^2$ depends only on the interval I, since the cross correlations Y_{IJ} have the same statistical properties for each segment J in I.

For each interval I, we calculate the mean, Y_I, and (sample) standard deviation, $s_{Y_{IJ}}$, of the 10 cross-correlation values Y_{IJ}:

$$Y_I \equiv \frac{1}{10} \sum_{J=1}^{10} Y_{IJ}, \quad (5.11)$$

$$s_{Y_{IJ}} \equiv \sqrt{\frac{1}{9} \sum_{J=1}^{10} (Y_{IJ} - Y_I)^2}. \quad (5.12)$$

We also form a *weighted* average, $Y_{\rm opt}$, of the Y_I over the whole run:

$$Y_{\rm opt} \equiv \frac{\sum_I \sigma_{Y_{IJ}}^{-2} Y_I}{\sum_I \sigma_{Y_{IJ}}^{-2}}. \quad (5.13)$$

The statistic $Y_{\rm opt}$ maximizes the expected signal-to-noise ratio for a stochastic signal, allowing for nonstationary detector noise from one 900-sec interval I to the next [18]. Dividing $Y_{\rm opt}$ by the time $T_{\rm seg}$ over which an individual cross-correlation measurement is made gives, in the absence of cross-correlated detector noise, an estimate of the stochastic background level:[9] $\hat{\Omega}_0 h_{100}^2 = Y_{\rm opt}/T_{\rm seg}$.

Finally, in Sec. V E we will be interested in the spectral properties of Y_{IJ}, Y_I, and $Y_{\rm opt}$. Thus, for later reference, we define:

$$\tilde{Y}_{IJ}[\ell] \equiv \tilde{Q}_I[\ell] \mathcal{G}_{IJ}[\ell], \quad (5.14)$$

$$\tilde{Y}_I[\ell] \equiv \frac{1}{10} \sum_{J=1}^{10} \tilde{Y}_{IJ}[\ell], \quad (5.15)$$

$$\tilde{Y}_{\rm opt}[\ell] \equiv \frac{\sum_I \sigma_{Y_{IJ}}^{-2} \tilde{Y}_I[\ell]}{\sum_I \sigma_{Y_{IJ}}^{-2}}. \quad (5.16)$$

Note that $2\,\mathrm{Re}\,\Sigma_{\ell=\ell_{\min}}^{\ell_{\max}} \delta f \cdot$ of the above quantities equal Y_{IJ}, Y_I, and $Y_{\rm opt}$, respectively.

[8] To make this correspondence with Eq. (4.3), the factor of 2 and real part in Eq. (5.5) are needed since we are summing only over *positive* frequencies, e.g., 40–314 Hz for the LHO-LLO correlation. Basically, integrals over continuous frequency are replaced by sums over discrete frequency bins using the correspondence $\int_{-\infty}^{\infty} df \to 2\,\mathrm{Re}\,\Sigma_{\ell=\ell_{\min}}^{\ell_{\max}} \delta f$.

[9] We use a hat $\hat{}$ to indicate an estimate of the actual (unknown) value of a quantity.

B. Windowing

In taking the discrete Fourier transform of the raw 90-sec data segments, care must be taken to limit the spectral leakage of large, low-frequency components into the sensitive band. In general, some combination of high-pass filtering in the time domain, and windowing prior to the Fourier transform can be used to deal with spectral leakage. In this analysis we have found it sufficient to apply an appropriate window to the data.

Examining the dynamic range of the data helps establish the allowed leakage. Figure 1 shows that the lowest instrument noise around 60 Hz is approximately $10^{-19}/\sqrt{\mathrm{Hz}}$ (for L1). While not shown in this plot, the rms level of the raw data corresponds to a strain of order 10^{-16}, and is due to fluctuations in the 10–30-Hz band. Leakage of these low-frequency components must be at least below the sensitive band noise level; e.g., leakage must be below 10^{-3} for a 30-Hz offset. A tighter constraint on the leakage comes when considering that these low-frequency components may be correlated between the two detectors, as they surely will be at some frequencies for the two interferometers at LHO, due to the common seismic environment. In this case the leakage should be below the predicted stochastic background sensitivity level, which is approximately 2.5 orders of magnitude below the individual detector noise levels for the LHO H1-H2 case. Thus, the leakage should be below 3×10^{-6} for a 30-Hz offset.

On the other hand, we prefer not to use a window that has an average value significantly less than unity (and correspondingly low leakage, such as a Hann window), because it will effectively reduce the amount of data contributing to the cross correlation. Provided that the windowing is sufficient to prevent significant leakage of power across the frequency range, the net effect is to multiply the expected value of the signal-to-noise ratio by $\overline{w_1 w_2}/\sqrt{\overline{w_1^2 w_2^2}}$ [cf. Eqs. (5.7),(5.8)].

For example, when w_1 and w_2 are both Hann windows, this factor is equal to $\sqrt{18/35}\approx0.717$, which is equivalent to reducing the data set length by a factor of 2. In principle one should be able to use overlapping data segments to avoid this effective loss of data, as in Welch's power spectrum estimation method. In this case, the calculations for the expected mean and variance of the cross correlations would have to take into account the statistical interdependence of the overlapping data.

Instead, we have used a Tukey window [39], which is essentially a Hann window split in half, with a constant section of all 1's in the middle. We can choose the length of the Hann portion of the window to provide sufficiently low leakage, yet maintain a unity value over most of the window. Figure 5 shows the leakage function of the Tukey window that we use (a 1-sec Hann window with an 89-sec flat section spliced into the middle), and compares it to Hann and rectangular windows. The Tukey window leakage is less than 10^{-7} for all frequencies greater than 35 Hz away from the FFT bin center. This is 4 orders of magnitude better than what is needed for the LHO-LLO correlations and a factor of 30 better suppression than needed for the H1-H2 correlation.

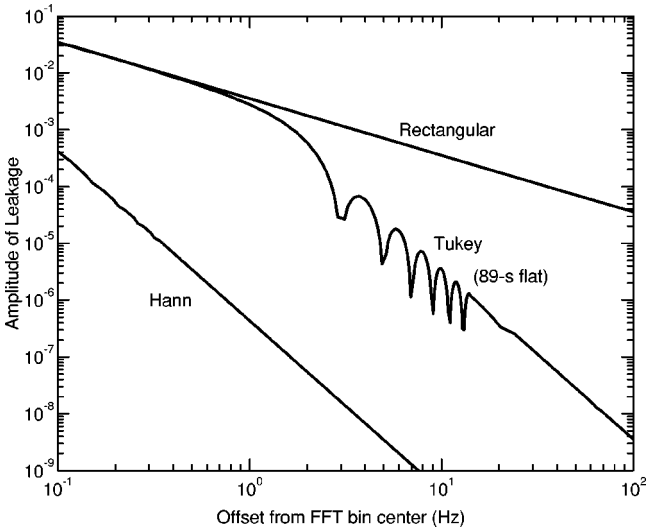

FIG. 5. Leakage function for a rectangular window, a standard Hann window of width 90 sec, and a Tukey window consisting of a 1-sec Hann window with an 89-sec flat section spliced into the middle. The curves show the envelope of the leakage functions, with a varying frequency resolution, so the zeros of the functions are not seen.

To explicitly verify that the Tukey window behaved as expected, we re-analyzed the H1-H2 data with a pure Hann window (see also Sec. VIII). The result of this re-analysis, properly scaled to take into account the effective reduction in observation time, was, within error, the same as the original analysis with a Tukey window. Since the H1-H2 correlation is the most prone of all correlations to spectral leakage (due to the likelihood of cross-correlated low-frequency noise components), the lack of a significant difference between the pure Hann and Tukey window analyses provided additional support for the use of the Tukey window.

C. Frequency band selection and discrete frequency elimination

In computing the discrete cross-correlation integral, we are free to restrict the sum to a chosen frequency region or regions; in this way the variance can be reduced (e.g., by excluding low frequencies where the detector power spectra are large and relatively less stationary), while still retaining most of the signal. We choose the frequency ranges by determining the band that contributes most of the expected signal-to-noise ratio, according to Eq. (4.11). Using the strain power spectra shown in Fig. 1, we compute the signal-to-noise ratio integral of Eq. (4.11) from a very low frequency (a few Hz) up to a variable cutoff frequency, and plot the resulting signal-to-noise ratio versus cutoff frequency (Fig. 6). For each interferometer pair, the lower band edge is chosen to be 40 Hz, while the upper band edge choices are 314 Hz for LHO-LLO correlations (where there is a zero in the overlap reduction function), and 300 Hz for H1-H2 correlations (chosen to exclude $\sim$340-Hz resonances in the test mass mechanical suspensions, which were not well resolved in the power spectra).

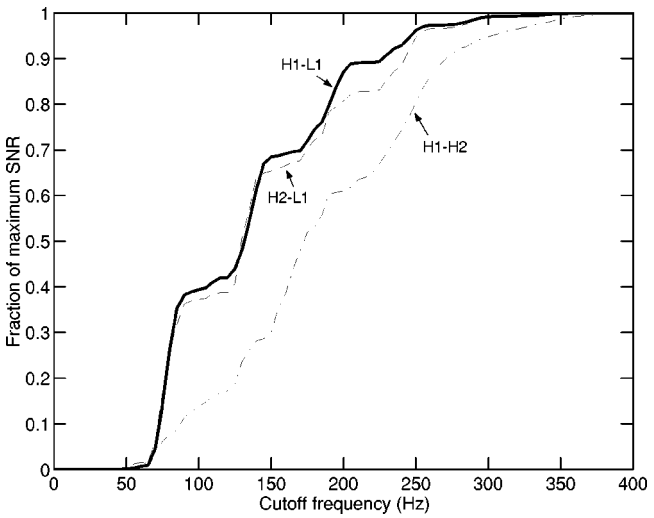

FIG. 6. Curves show the fraction of maximum expected signal-to-noise ratio as a function of cutoff frequency, for the three interferometer pairs. The curves were made by numerically integrating Eq. (4.11) from a few Hz up to the variable cutoff frequency, using the strain sensitivity spectra shown in Fig. 1.

Within the 40–314 (300)-Hz band, discrete frequency bins at which there are known or potential instrumental correlations due to common periodic sources are eliminated from the cross-correlation sum. For example, a significant feature in all interferometer outputs is a set of spectral lines extending out to beyond 2 kHz, corresponding to the 60-Hz power line and its harmonics (n60-Hz lines). Since these lines obviously have a common source—the mains power supplying the instrumentation—they are potentially correlated between detectors. To avoid including any such correlation in the analysis, we eliminate the n60-Hz frequency bins from the sum in Eq. (5.5).

Another common periodic signal arises from the data acquisition timing systems in the detectors. The absolute timing and synchronization of the data acquisition systems between detectors is based on 1 pulse-per-second signals produced by Global Positioning System (GPS) receivers at each site. In each detector, data samples are stored temporarily in 1/16-sec buffers, prior to being collected and written to disk. The process, through mechanisms not yet established, results in some power at 16 Hz and harmonics in the detectors' output data channels. These signals are extremely narrow band and, due to the stability and common source of the GPS-derived timing, can be correlated between detectors. To avoid including any of these narrow-band correlations, we eliminate the n16-Hz frequency bins from the sum in Eq. (5.5).

Finally, there may be additional correlated narrow-band features due to highly stable clocks or oscillators that are common components among the detectors (e.g., computer monitors can have very stable sync rates, typically at 70 Hz). To describe how we avoid such features, we first present a quantitative analysis of the effect of coherent spectral lines on our cross-correlation measurement. We begin by following the treatment of correlated detector noise given in Sec. V E of Ref. [18]. The contribution of cross-correlated detector noise to the cross correlation Y will be small compared to the intrinsic measurement noise if

$$\left|\frac{T}{2}\int_{-\infty}^{\infty} df P_{12}(|f|)\tilde{Q}(f)\right| \ll \sigma_Y, \tag{5.17}$$

where $P_{12}(|f|)$ is the cross-power spectrum of the strain noise (n_1,n_2) in the two detectors, T is the total observation time, and σ_Y is defined by Eq. (4.6). Using Eq. (4.8), this condition becomes

$$\mathcal{N}\left|\int_{-\infty}^{\infty} df \frac{P_{12}(|f|)\gamma(|f|)}{|f|^3 P_1(|f|)P_2(|f|)}\right| \ll \frac{2\sigma_Y}{T}, \tag{5.18}$$

or, equivalently,

$$\frac{3H_{100}^2}{5\pi^2}\left|\int_{-\infty}^{\infty} df \frac{P_{12}(|f|)\gamma(|f|)}{|f|^3 P_1(|f|)P_2(|f|)}\right| \ll 2\sigma_Y^{-1}, \tag{5.19}$$

where Eqs. (4.9),(4.10) were used to eliminate $\mathcal{N}$ in terms of σ_Y^2:

$$\mathcal{N} = \frac{3H_{100}^2}{5\pi^2}\frac{\sigma_Y^2}{T}. \tag{5.20}$$

Now consider the presence of a correlated periodic signal, such that the cross spectrum $P_{12}(f)$ is significant only at a single (positive) discrete frequency, f_L. For this component to have a small effect, the above condition becomes:

$$\frac{3H_{100}^2}{5\pi^2}\left|\Delta f \frac{P_{12}(f_L)\gamma(f_L)}{f_L^3 P_1(f_L)P_2(f_L)}\right| \ll \sigma_Y^{-1}, \tag{5.21}$$

where Δf is the frequency resolution of the discrete Fourier transform used to approximate the frequency integrals. The left-hand-side of Eq. (5.21) can be expressed in terms of the coherence function $\Gamma_{12}(f)$, which is essentially a normalized cross spectrum, defined as [40]:

$$\Gamma_{12}(f) \equiv \frac{|P_{12}(f)|^2}{P_1(f)P_2(f)}. \tag{5.22}$$

The condition on the coherence at f_L is thus

$$[\Gamma_{12}(f_L)]^{1/2} \ll \frac{\sigma_Y^{-1}}{\Delta f}\frac{5\pi^2}{3H_{100}^2}\frac{\sqrt{P_1(f_L)P_2(f_L)}}{|f_L^{-3}\gamma(f_L)|}. \tag{5.23}$$

Since σ_Y increases as $T^{1/2}$, the limit on the coherence $\Gamma_{12}(f_L)$ becomes smaller as $1/T$. To show how this condition applies to the S1 data, we estimate the factors in Eq. (5.23) for the H2-L1 pair, focusing on the band 100–150 Hz. We assume any correlated spectral line is weak enough that it does not appear in the power spectrum estimates used to construct the optimal filter. Noting that the combination $(3H_{100}^2/10\pi^2)f^{-3}$ is just the power spectrum of gravitational waves $S_{\rm gw}(f)$ with $\Omega_0 h_{100}^2 = 1$ [cf. Eq. (3.6)], we can evaluate the right-hand side of Eq. (5.23) by estimating the ratios $[P_i/S_{\rm gw}]^{1/2}$ from Fig. 1 for $\Omega_0 h_{100}^2 = 1$. Within the band

100–150 Hz, this gives: $(P_1P_2)^{1/2}/S_{\rm gw} \gtrsim 2500$. The overlap reduction function in this band is $|\gamma| \lesssim 0.05$. The appropriate frequency resolution Δf is that corresponding to the 90-sec segment discrete Fourier transforms, so $\Delta f = 0.011$ Hz. As described later in Sec. VI, we calculate a statistical error, σ_Ω, associated with the stochastic background estimate $Y_{\rm opt}/T_{\rm seg}$. Under the implicit assumption made in Eq. (5.23) that the detector noise is stationary, one can show that $\sigma_Y = T\sigma_\Omega$. Finally, referring to Table IV for an estimate of σ_Ω, and using the total H2-L1 observation time of 51 h, we obtain $\sigma_Y \approx 2.8\times 10^6$ sec. Thus, the condition of Eq. (5.23) becomes: $[\Gamma_{12}(f_L)]^{1/2} \ll 1$.

Using this example estimate as a guide, specific lines are rejected by calculating the coherence function between detector pairs for the full sets of analyzed S1 data, and eliminating any frequency bins at which $\Gamma_{12}(f_L) \geqslant 10^{-2}$. The coherence functions are calculated with a frequency resolution of 0.033 Hz, and approximately 20 000 (35 000) averages for the LHO-LLO (LHO-LHO) pairs, corresponding to statistical uncertainty levels $\sigma_\Gamma \equiv 1/N_{\rm avg}$ of approximately 5×10^{-5} (3×10^{-5}). The exclusion threshold thus corresponds to a cut on the coherence data of order 100 σ_Γ.

For the H2-L1 pair, this procedure results in eliminating the 250-Hz frequency bin, whose coherence level was about 0.02; the H2-L1 coherence function over the analysis band is shown in Fig. 7. For H1-H2, the bins at 168.25 Hz and 168.5 Hz were eliminated, where the coherence was also about 0.02 (see Fig. 17). The sources of these lines are unknown. For H1-L1, no additional frequencies were removed by the coherence threshold (see Fig. 8).

It is worth noting that correlations at the n60-Hz lines are suppressed even without explicitly eliminating these frequency bins from the sum. This is because these frequencies have a high signal-to-noise ratio in the power spectrum estimates, and thus they have relatively small values in the optimal filter. The optimal filter thus tends to suppress spectral lines that show up in the power spectra. This effect is illustrated in Fig. 9, and is essentially the result of having four powers of $\tilde{s}_i(f)$ in the denominator of the integrand of the cross correlation, but only two powers in the numerator. Nonetheless, we chose to remove the n60-Hz bins from the cross-correlation sum for robustness, and as good practice for future analyses, where improvements in the electronics instrumentation may reduce the power line coupling such that the optimal filter suppression is insufficient.

Such optimal filter suppression does not occur, however, for the 16-Hz line and its harmonics, and the additional 168.25-, 168.5-, 250-Hz lines; these lines typically do not appear in the power spectrum estimates, or do so only with a small signal-to-noise ratio. These lines must be explicitly eliminated from the cross-correlation sum. These discrete frequency bins are all zeroed out in the optimal filter, so that each excluded frequency removes 0.25 Hz of bandwidth from the calculation.

D. Results and interpretation

The primary goal of our analysis is to set an upper limit on the strength of a stochastic gravitational wave background. The cross-correlation measurement is, in principle, sensitive to a combination of a stochastic gravitational background and instrumental noise that is correlated between two detectors. In order to place an upper limit on a gravitational wave background, we must have confidence that instrumental correlations are not playing a significant role. Gaining such confidence for the correlation of the two LHO interferometers may be difficult, in general, as they are both exposed to many of the same environmental disturbances. In fact, for the S1 analysis, a strong (negative) correlation *was* observed between the two Hanford interferometers, thus preventing us from setting an upper limit on $\Omega_0 h_{100}^2$ using the H1-H2 pair results. The correlated instrumental noise sources, relatively broadband compared to the excised narrow-band features described in the previous section, produced a significant H1-H2 cross correlation (signal-to-noise ratio of -8.8); see Sec. VIII for further discussion of the H1-H2 instrumental correlations.

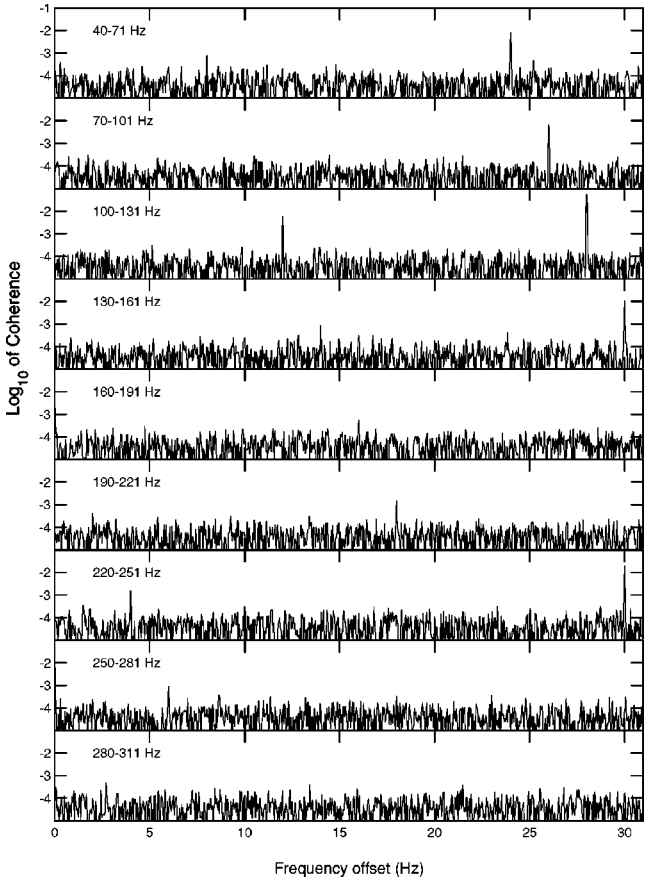

FIG. 7. Coherence between the H2 and L1 detector outputs during S1. The coherence is calculated with a frequency resolution of 0.033 Hz and $N_{\rm avg} \approx 20\,000$ periodogram averages (50% overlap); Hann windows are used in the Fourier transforms. There are significant peaks at harmonics of 16 Hz (data acquisition buffer rate) and at 250 Hz (unknown origin). These frequencies are all excluded from the cross-correlation sum. The broadband coherence level corresponds to the expected statistical uncertainty level of $1/N_{\rm avg} \approx 5\times 10^{-5}$.

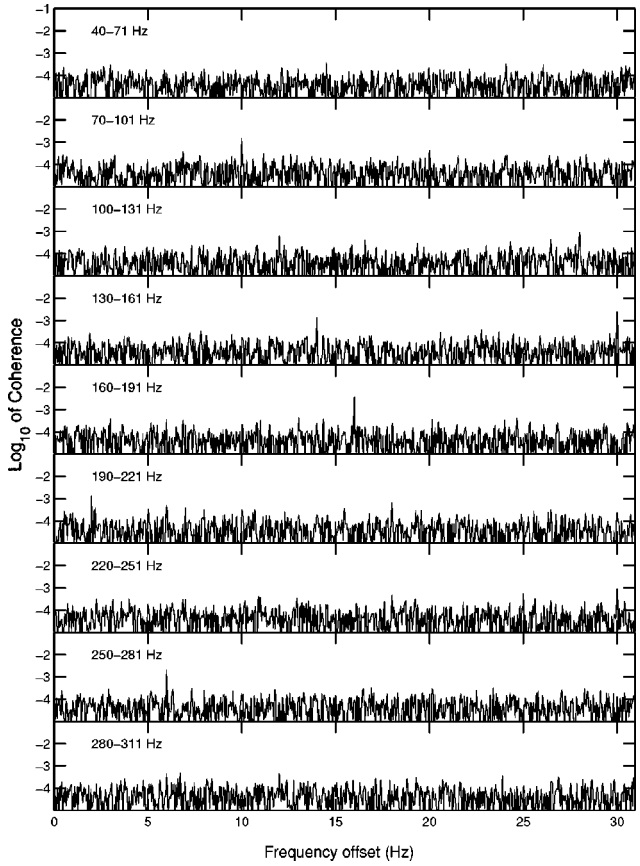

FIG. 8. Coherence between the H1 and L1 detector outputs during S1, calculated as described in the caption of Fig. 7. There are significant peaks at harmonics of 16 Hz (data acquisition buffer rate). These frequencies are excluded from the cross-correlation sum. The broadband coherence level corresponds to the expected statistical uncertainty level of $1/N_{\mathrm{avg}} \approx 5 \times 10^{-5}$.

On the other hand, for the widely separated (LHO-LLO) interferometer pairs, there are only a few paths through which instrumental correlations could arise. Narrow-band inter-site correlations are seen, as described in the previous section, but the described measures have been taken to exclude them from the analysis. Seismic and acoustic noise in the several to tens of Hz band have characteristic coherence lengths of tens of meters or less, compared to the 3000-km LHO-LLO separation, and pose little problem. Globally correlated magnetic field fluctuations have been identified in the past as the most likely candidate capable of producing broadband correlated noise in the widely separated detectors [34]. An order-of-magnitude analysis of this effect was made in Ref. [18], concluding that correlated field fluctuations during magnetically noisy periods (such as during thunderstorms) could produce a LHO-LLO correlated strain signal corresponding to a stochastic gravitational background $\Omega_0 h_{100}^2$ of order 10^{-8}. These estimates evaluated the forces produced on the test masses by the correlated magnetic fields, via magnets that are bonded to the test masses to provide position and orientation control.[10] Direct tests made on the LIGO interferometers indicate that the magnetic field coupling to the strain signal was generally much higher during S1—up to 10^2 times greater for a single interferometer—than these force coupling estimates. Nonetheless, the correspondingly modified estimate of the equivalent Ω due to correlated magnetic fields is still 5 orders of magnitude below our present sensitivity. Indeed, Figs. 7 and 8 show no evidence of any significant broadband instrumental correlations in the S1 data. We thus set upper limits on $\Omega_0 h_{100}^2$ for both the H1-L1 and the H2-L1 pair results.

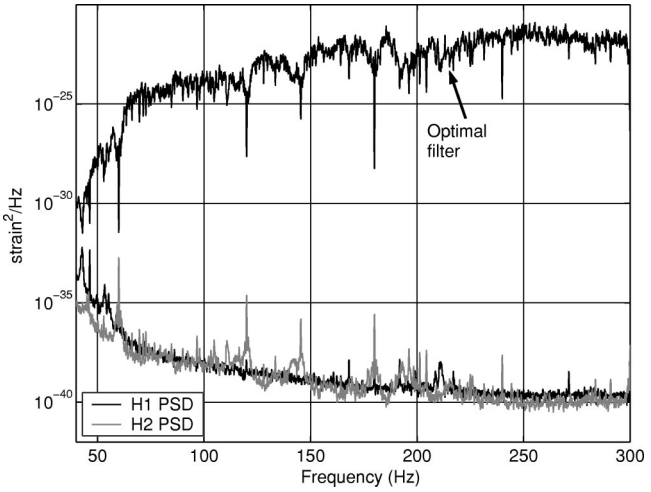

FIG. 9. Power spectral densities and optimal filter for the H1-H2 detector pair, using the sensitivities shown in Fig. 1. A scale factor has been applied to the optimal filter for display purposes. Note that spectral lines at 60 Hz and harmonics produce corresponding deep ''notches'' in the optimal filter.

Accounting for the combination of a gravitational wave background and instrumental correlations, we define an *effective* Ω, denoted Ω_{eff}, for which our measurement $Y_{\mathrm{opt}}/T_{\mathrm{seg}}$ provides an estimate:

$$\hat{\Omega}_{\mathrm{eff}} h_{100}^2 \equiv Y_{\mathrm{opt}}/T_{\mathrm{seg}} = (\hat{\Omega}_0 + \hat{\Omega}_{\mathrm{inst}}) h_{100}^2 . \qquad (5.24)$$

Note that Ω_{inst} (associated with instrumental correlations) may be either positive or negative, while Ω_0 for the gravitational wave background must be non-negative. We calculate a standard two-sided, frequentist 90% confidence interval on $\Omega_{\mathrm{eff}} h_{100}^2$ as follows:

$$[\hat{\Omega}_{\mathrm{eff}} h_{100}^2 - 1.65 \hat{\sigma}_{\Omega,\mathrm{tot}}, \hat{\Omega}_{\mathrm{eff}} h_{100}^2 + 1.65 \hat{\sigma}_{\Omega,\mathrm{tot}}] \qquad (5.25)$$

where $\hat{\sigma}_{\Omega,\mathrm{tot}}$ is the total estimated error of the cross-correlation measurement, as explained in Sec. VI. In a fre-

[10]The actual limit on $\Omega_0 h_{100}^2$ that appears in Ref. [18] is 10^{-7}, since the authors assumed a magnetic dipole moment of the test mass magnets that is a factor of 10 higher than what is actually used.

TABLE II. Measured 90% confidence intervals and upper limits for the three LIGO interferometer pairs, assuming $\Omega_{\rm gw}(f) \equiv \Omega_0 = \text{const}$ in the specified frequency band. For all three pairs we compute a confidence interval according to Eq. (5.25). For the LHO-LLO pairs, we are confident in assuming the instrumental correlations are insignificant, and an upper limit on a stochastic gravitational background is computed according to Eq. (5.26). Our established upper limit comes from the H2-L1 pair. The $\pm$ error bars given for the confidence intervals and upper limit values derive from a $\pm 10\%$ uncertainty in the calibration magnitude of each detector; see Sec. VI and Table IV. The $\chi^2_{\rm min}$ per degree of freedom values are the result of a frequency-domain comparison between the measured and theoretically expected cross correlations, described in Sec. V E.

Interferometer pair	$\hat{\Omega}_{\rm eff} h_{100}^2$	$\hat{\Omega}_{\rm eff} h_{100}^2 / \hat{\sigma}_{\Omega,\rm tot}$	90% confidence interval on $\Omega_{\rm eff} h_{100}^2$	90% confidence upper limit	$\chi^2_{\rm min}$ (per dof)	Frequency range	Observation time
H1-H2	-8.3	-8.8	$[-9.9 \pm 2.0, -6.8 \pm 1.4]$		4.9	40–300 Hz	100.25 h
H1-L1	32	1.8	$[2.1 \pm .42, 61 \pm 12]$	$\Omega_0 h_{100}^2 \leqslant 55 \pm 11$	0.96	40–314 Hz	64 h
H2-L1	0.16	0.0094	$[-30 \pm 6.0, 30 \pm 6.0]$	$\Omega_0 h_{100}^2 \leqslant 23 \pm 4.6$	1.0	40–314 Hz	51.25 h

quentist interpretation, this means that if the experiment were repeated many times, generating many values of $\hat{\Omega}_{\rm eff} h_{100}^2$ and $\hat{\sigma}_{\Omega,\rm tot}$, then the true value of $\Omega_{\rm eff} h_{100}^2$ is expected to lie within 90% of these intervals. We establish such a confidence interval for each detector pair.

For the H1-L1 and H2-L1 detector pairs, we are confident in assuming that systematic broad-band instrumental cross correlations are insignificant, so the measurement of $\hat{\Omega}_{\rm eff} h_{100}^2$ is used to establish an upper limit on a stochastic gravitational wave background. Specifically, assuming Gaussian statistics with fixed rms deviation, $\hat{\sigma}_{\Omega,\rm tot}$, we set a standard 90% confidence level upper limit on $\Omega_0 h_{100}^2$. Since the actual value of Ω_0 must be non-negative, we set the upper limit to $1.28 \hat{\sigma}_{\Omega,\rm tot}$ if the measured value of $\hat{\Omega}_{\rm eff} h_{100}^2$ is less than zero.[11] Explicitly,

$$\Omega_0 h_{100}^2 \leqslant \max\{\hat{\Omega}_{\rm eff} h_{100}^2, 0\} + 1.28 \hat{\sigma}_{\Omega,\rm tot}. \qquad (5.26)$$

Table II summarizes the results obtained in applying the cross-correlation analysis to the LIGO S1 data. The most constraining (i.e., smallest) upper limit on a gravitational wave stochastic background comes from the H2-L1 detector pair, giving $\Omega_0 h_{100}^2 \leqslant 23$. Using Eq. (3.6), this can also be expressed as an upper limit on the stochastic background power spectrum (taking $h_{100} = 0.73$): $S_{\rm gw}(f) < 3.8 \times 10^{-42}\ (100\ {\rm Hz}/f)^3 {\rm Hz}^{-1}$.

The significant H1-H2 instrumental correlation is discussed further in Sec. VIII. The upper limits in Table II can be compared with the expectations given in Fig. 1, properly scaling the latter for the actual observation times. The H2-L1 expected upper limit for 50 h of data would be $\Omega_0 h_{100}^2 \leqslant 14$. The difference between this number and our result of 23 is due to the fact that, on average, the detector strain sensitivities were poorer than those shown in Fig. 1.

[11]We are assuming here that a negative value of $\hat{\Omega}_{\rm eff} h_{100}^2$ is due to random statistical fluctuations in the detector outputs and not to systematic instrumental correlations.

In computing the Table II numbers, some data selection has been performed to remove times of higher than average detector noise. Specifically, the theoretical variances of all 900-sec intervals are calculated, and the sum of the $\sigma_{Y_{IJ}}^{-2}$ is computed. We then select the set of largest $\sigma_{Y_{IJ}}^{-2}$ (i.e., the most sensitive intervals) that accumulate 95% of the sum of all the weighting factors, and include only these intervals in the Table II results. This selection includes 75–85 % of the analyzed data, depending on the detector pair. We also excluded an additional ~ 10 h of H2 data near the beginning of S1 because of large data acquisition system timing errors during this period. The deficits between the observation times given in Table II and the total S1 double-coincident times given in Sec. II are due to a combination of these and other selections, spelled out in Table III.

Shown in Fig. 10 are the weighting factors $\sigma_{Y_{IJ}}^{-2}$ [cf. Eq. (5.8)] over the duration of the S1 run. The $\sigma_{Y_{IJ}}^{-2}$ enter the expression for $Y_{\rm opt}$ [Eq. (5.13)] and give a quantitative measure of the sensitivity of a pair of detectors to a stochastic gravitational wave background during the Ith interval. Addi-

TABLE III. Summary of the selection criteria applied to the double-coincidence data for S1. ***A:*** portion of the 408-h S1 run having double-coincidence stretches greater than 600 sec; ***B:*** data portion satisfying criterion *A*, plus: data length is $\geqslant 900$ sec for the analysis pipeline, *and* the calibration monitoring was operational; ***C:*** data portion satisfying criterion *B*, plus: GPS timing is valid *and* calibration data are within bounds; ***D:*** data portion satisfying criterion *C*, plus: quietest data intervals that accumulate 95% of the sum of the weighting factors. This last data set was used in the analysis pipeline.

Selection criteria	H1-H2	H1-L1	H2-L1
A: All double-	188 h	116 h	131 h
coincidence data	46%	28%	32%
B: A plus $T_{\rm lock} > 900$ sec,	134 h	75 h	81 h
and calibration monitored	33%	18%	20%
C: B plus valid GPS timing,	119 h	75 h	66 h
and calibrations within bounds	29%	18%	16%
D: C plus quietest	100 h	64 h	51 h
intervals	25%	16%	13%

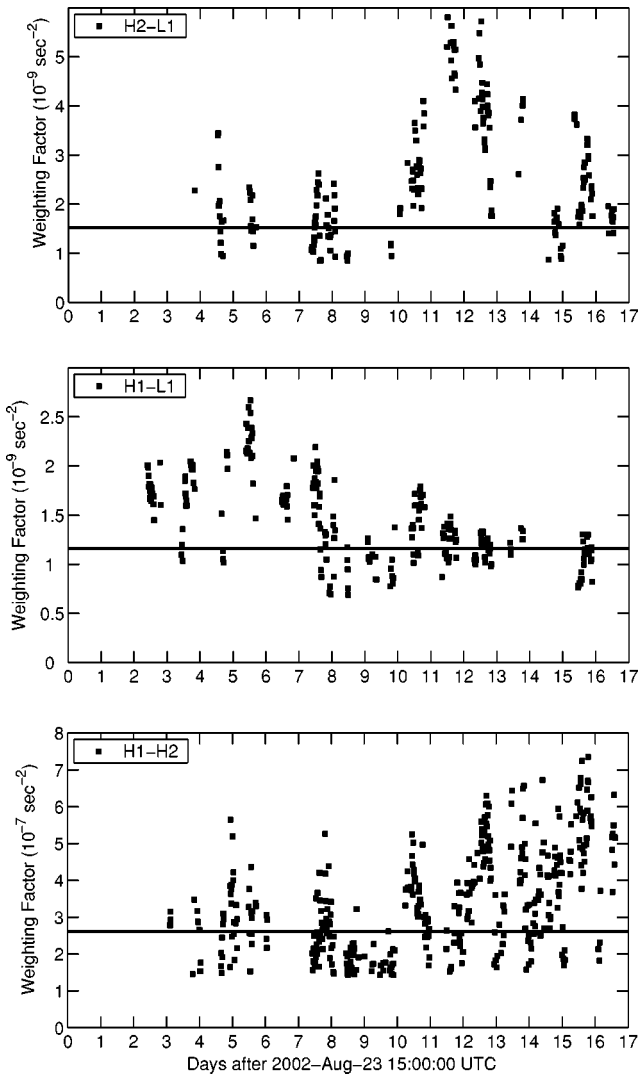

FIG. 10. The weighting factors $\sigma_{Y_{IJ}}^{-2}$ for each interferometer pair over the course of the S1 run; each point represents 900 sec of data. In each plot, a horizontal line indicates the weighting factor corresponding to the detector power spectra averaged over the whole run.

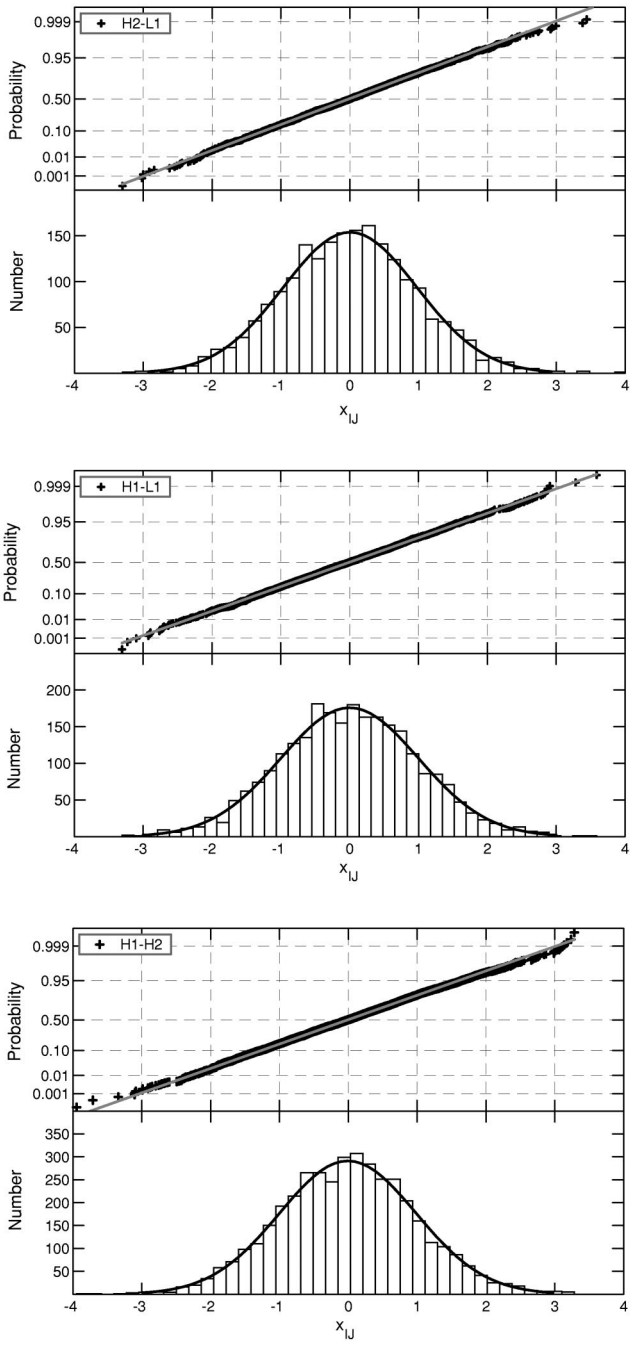

FIG. 11. Normal probabilities and histograms of the values $x_{IJ} \equiv (Y_{IJ} - Y_{\mathrm{opt}})/\sigma_{Y_{IJ}}$, for all I,J included in the Table II results. In theory, these values should be drawn from a Gaussian distribution of zero mean and unit variance. The solid lines indicate the Gaussian that best fits the data; in the cumulative probability plots, curvature away from the straight lines is a sign of non-Gaussian statistics.

tionally, to gauge the accuracy of the weighting factors, we compared the theoretical standard deviations $\sigma_{Y_{IJ}}$ to the measured standard deviations $s_{Y_{IJ}}$ [cf. Eq. (5.12)]. For each interferometer pair, all but one or two of the $\sigma_{Y_{IJ}}/s_{Y_{IJ}}$ ratios lie between 0.5 and 2, and show no systematic trend above or below unity.

Finally, Fig. 11 shows the distribution of the cross-correlation values with mean removed and normalized by the theoretical standard deviations—i.e., $x_{IJ} \equiv (Y_{IJ} - Y_{\mathrm{opt}})/\sigma_{Y_{IJ}}$. The values follow quite closely the expected Gaussian distributions.

E. Frequency- and time-domain characterization

Because of the broadband nature of the interferometer strain data, it is possible to explore the frequency-domain character of the cross correlations. In the analysis pipeline, we keep track of the individual frequency bins that contribute to each Y_{IJ}, and form the weighted sum of frequency bins over the full processed data to produce an aggregate cross-correlation spectrum, $\tilde{Y}_{\mathrm{opt}}[l]$, for each detector pair [cf. Eq. (5.16)]. These spectra, along with their cumulative

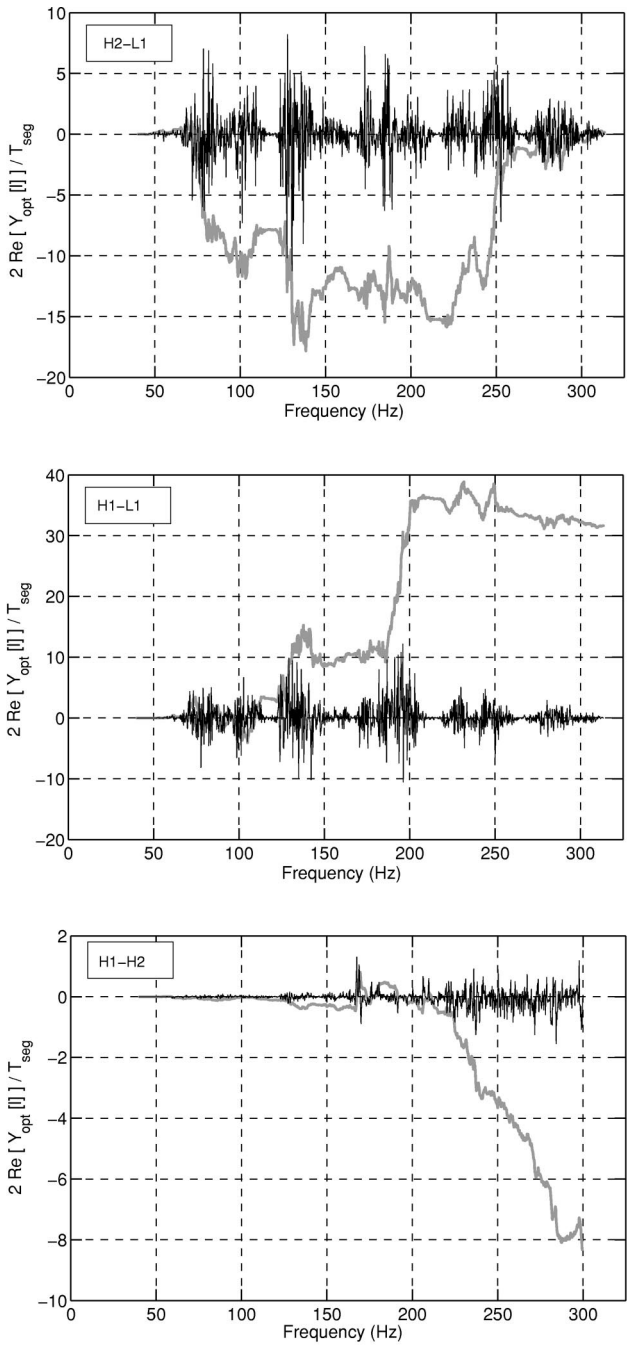

FIG. 12. Real part of the cross-correlation spectrum, $\tilde{Y}_{\rm opt}[\ell]/T_{\rm seg}$ (units of Hz^{-1}), for each detector pair. The gray line in each plot shows the cumulative sum of the spectrum from 40 Hz to f_ℓ, multiplied by δf (which makes it dimensionless); the value of this curve at the right end is our estimate $\hat{\Omega}_{\rm eff}h_{100}^2$. Note that the excursions in the cumulative sum for the H1-L1 and H2-L1 correlations have magnitudes less than 1–2 error bars of the corresponding point estimates; simulations with uncorrelated data show the same qualitative behavior.

sums, are shown in Fig. 12. $\tilde{Y}_{\rm opt}[\ell]$ can be quantitatively compared to the theoretically expected signal arising from a stochastic background with $\Omega_{\rm gw}(f)\equiv\Omega_0=$const by forming the χ^2 statistic:

$$\chi^2(\Omega_0)\equiv\sum_{\ell=\ell_{\rm min}}^{\ell_{\rm max}}\frac{[\mathrm{Re}(\tilde{Y}_{\rm opt}[\ell])-\mu_{\tilde{Y}_{\rm opt}}[\ell]]^2}{\sigma^2_{\tilde{Y}_{\rm opt}}[\ell]}, \quad (5.27)$$

which is a quadratic function of Ω_0. The sum runs over the $\sim$1000 frequency bins[12] contained in each spectra. The expected values $\mu_{\tilde{Y}_{\rm opt}}[\ell]$ and theoretical variances $\sigma^2_{\tilde{Y}_{\rm opt}}[\ell]$ are given by

$$\mu_{\tilde{Y}_{\rm opt}}[\ell]\equiv\Omega_0\frac{T_{\rm seg}}{2}\frac{3H_0^2}{10\pi^2}\overline{w_1w_2}\times\frac{\sum_I\sigma_{Y_{IJ}}^{-2}\mathcal{N}_I\dfrac{\gamma^2[\ell]}{f_\ell^6P_{1I}[\ell]P_{2I}[\ell]}}{\sum_I\sigma_{Y_{IJ}}^{-2}}, \quad (5.28)$$

$$\sigma^2_{\tilde{Y}_{\rm opt}}[\ell]\equiv\frac{1}{10}\frac{T_{\rm seg}}{4}\overline{w_1^2w_2^2}\frac{\sum_I\sigma_{Y_{IJ}}^{-4}\mathcal{N}_I^2\dfrac{\gamma^2[\ell]}{f_\ell^6P_{1I}[\ell]P_{2I}[\ell]}}{\left(\sum_I\sigma_{Y_{IJ}}^{-2}\right)^2}. \quad (5.29)$$

Note that by using Eqs. (5.7),(5.8), one can show

$$2\sum_{\ell=\ell_{\rm min}}^{\ell_{\rm max}}\delta f\,\mu_{\tilde{Y}_{\rm opt}}[\ell]=\Omega_0h_{100}^2T_{\rm seg}, \quad (5.30)$$

$$2\sum_{\ell=\ell_{\rm min}}^{\ell_{\rm max}}\delta f\,\sigma^2_{\tilde{Y}_{\rm opt}}[\ell]=\frac{1}{10}\left(\sum_I\sigma_{Y_{IJ}}^{-2}\right)^{-1}, \quad (5.31)$$

which are the expected value and theoretical variance of the weighted cross correlation $Y_{\rm opt}$ [cf. Eq. (5.13)].

For each detector pair, we find that the minimum χ^2 value occurs at the corresponding estimate $\hat{\Omega}_{\rm eff}h_{100}^2$ for that pair, and the width of the $\chi^2=\chi^2_{\rm min}\pm2.71$ points corresponds to the 90% confidence intervals given in Table II. For the H1-L1 and H2-L1 pairs, the minimum values are $\chi^2_{\rm min}=(0.96,1.0)$ per degree of freedom. This results from the low signal-to-noise ratio of the measurements: $\hat{\Omega}_{\rm eff}h_{100}^2/\hat{\sigma}_{\Omega,\rm tot}=(1.8,.0094)$.

For the H1-H2 pair, $\chi^2_{\rm min}=4.9$ per degree of freedom. In this case the magnitude of the cross-correlation signal-to-noise ratio is relatively high, $\hat{\Omega}_{\rm eff}h_{100}^2/\hat{\sigma}_{\Omega,\rm tot}=-8.8$, and the value of $\chi^2_{\rm min}$ indicates the very low likelihood that the measurement is consistent with the stochastic background model. For $\sim$1000 frequency bins (the number of degrees of freedom of the fit), the probability of obtaining such a high value of $\chi^2_{\rm min}$ is extremely small, indicating that the source of the

[12]To be exact, 1020 frequency bins were used for the H1-L1, H2-L1 correlations and 1075 bins for H1-H2.

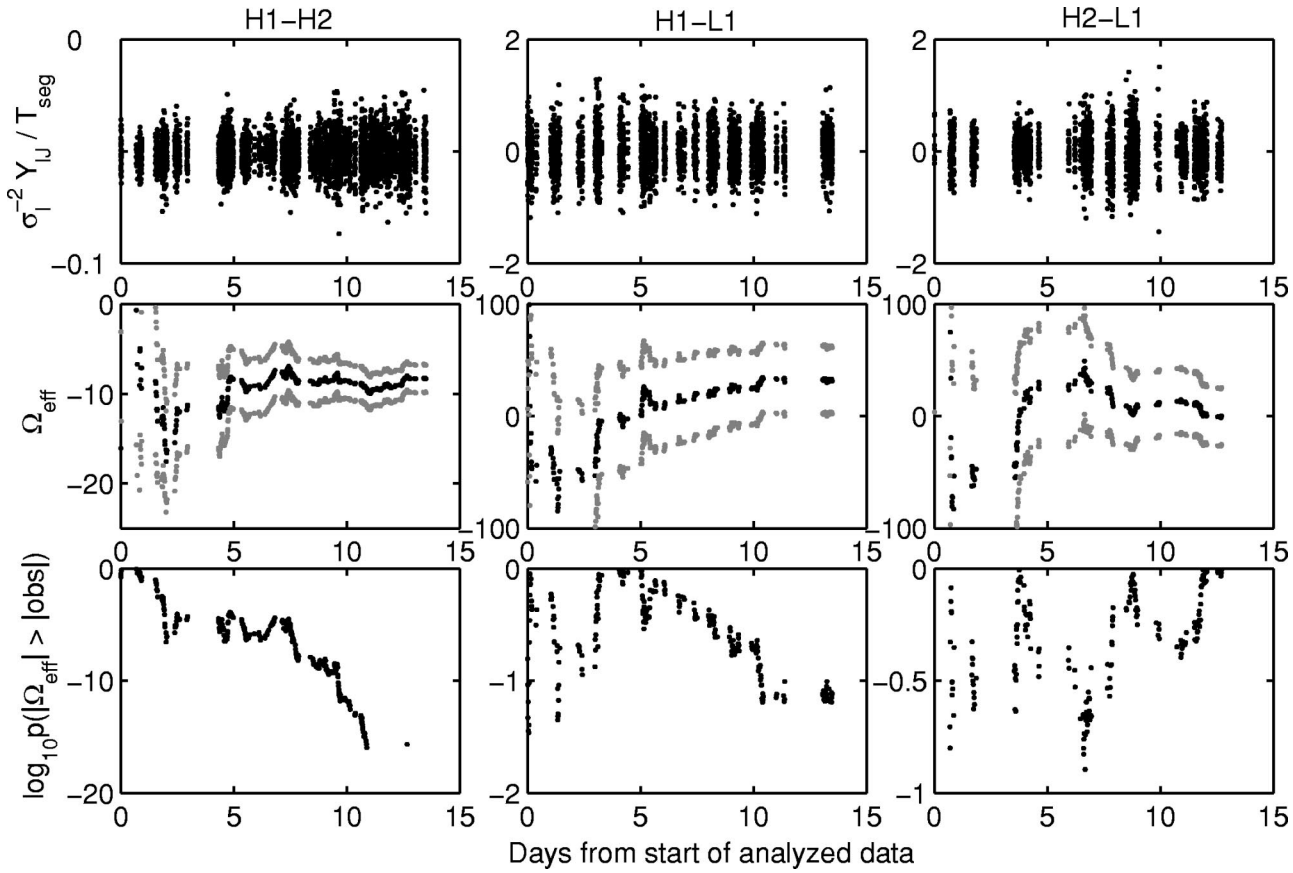

FIG. 13. Cross-correlation statistics as a function of amount of data analyzed. Each column of plots shows the analysis results for a given detector pair, as indicated, over the duration of the data set. Top plots: Points correspond to the cross-correlation statistic values Y_{IJ} appropriately normalized, $MT_{\rm seg}^{-1}\sigma_{Y_{IJ}}^{-2}Y_{IJ}/\Sigma_I\sigma_{Y_{IJ}}^{-2}$, where M is the total number of analyzed intervals, so that the mean of all the values is the final point estimate $\hat{\Omega}_{\rm eff}h_{100}^2$. The scatter shows the variation in the point estimates from segment to segment. Middle plots: Evolution over time of the estimated value of $\Omega_{\rm eff}h_{100}^2$. The black points give the estimates $\hat{\Omega}_{\rm eff}h_{100}^2$ and the gray points give the $\pm 1.65\hat{\sigma}_\Omega$ errors (90% confidence bounds), where $\hat{\sigma}_\Omega$ is defined by Eq. (6.1). The errors decrease with time, as expected from a $T^{-1/2}$ dependence on observation time. Bottom plots: Assuming that the estimates shown in the middle plots are drawn from zero-mean Gaussian random variables with the error bars indicated, the probability of obtaining a value of $|\Omega_{\rm eff}h_{100}^2| \geqslant$ observed absolute value is given by: $p(|\Omega_{\rm eff}h_{100}^2| \geqslant |x|) = 1 - {\rm erf}(|x|/\sqrt{2}\hat{\sigma}_\Omega)$. This is plotted in the bottom plots. For the H1-H2 pair, the probability becomes $< 10^{-20}$ after approximately 11 days. While the H1-L1 pair shows a signal-to-noise ratio above unity, $\hat{\Omega}_{\rm eff}h_{100}^2/\hat{\sigma}_{\Omega,{\rm tot}} = 1.8$, there is a 10% probability of obtaining an equal or larger value from random noise alone.

observed H1-H2 correlation is not consistent with a stochastic gravitational wave background having $\Omega_{\rm gw}(f) \equiv \Omega_0 = {\rm const}$.

It is also interesting to examine how the cross correlation behaves as a function of the volume of data analyzed. Figure 13 shows the weighted cross-correlation statistic values versus time, and the evolution of the estimate $\hat{\Omega}_{\rm eff}h_{100}^2$ and statistical error bar $\hat{\sigma}_\Omega$ over the data run. Also plotted are the probabilities $p(|\Omega_{\rm eff}h_{100}^2| \geqslant |x|) = 1 - {\rm erf}(|x|/\sqrt{2}\hat{\sigma}_\Omega)$ of obtaining a value of $\Omega_{\rm eff}h_{100}^2$ greater than or equal to the observed value, assuming that these values are drawn from a zero-mean Gaussian random distribution, of width equal to the cumulative statistical error at each point in time. For the H1-L1 and H2-L1 detector pairs, the probabilities are $\gtrsim 10\%$ for the majority of the run. For H1-H2, the probability drops below 10^{-20} after about 11 days, suggesting the presence of a nonzero instrumental correlation (see also Sec. VIII).

F. Time shift analysis

It is instructive to examine the behavior of the cross correlation as a function of a relative time shift τ introduced between the two data streams:

$$Y(\tau) \equiv \int_{-T/2}^{T/2} dt_1 \int_{-T/2}^{T/2} dt_2 s_1(t_1 - \tau) Q(t_1 - t_2) s_2(t_2)$$

$$= \int_{-\infty}^{\infty} df e^{i2\pi f\tau} \tilde{Y}(f), \tag{5.32}$$

where

$$\tilde{Y}(f) \equiv \int_{-\infty}^{\infty} df' \delta_T(f - f') \tilde{s}_1^*(f) \tilde{Q}(f') \tilde{s}_2(f'). \tag{5.33}$$

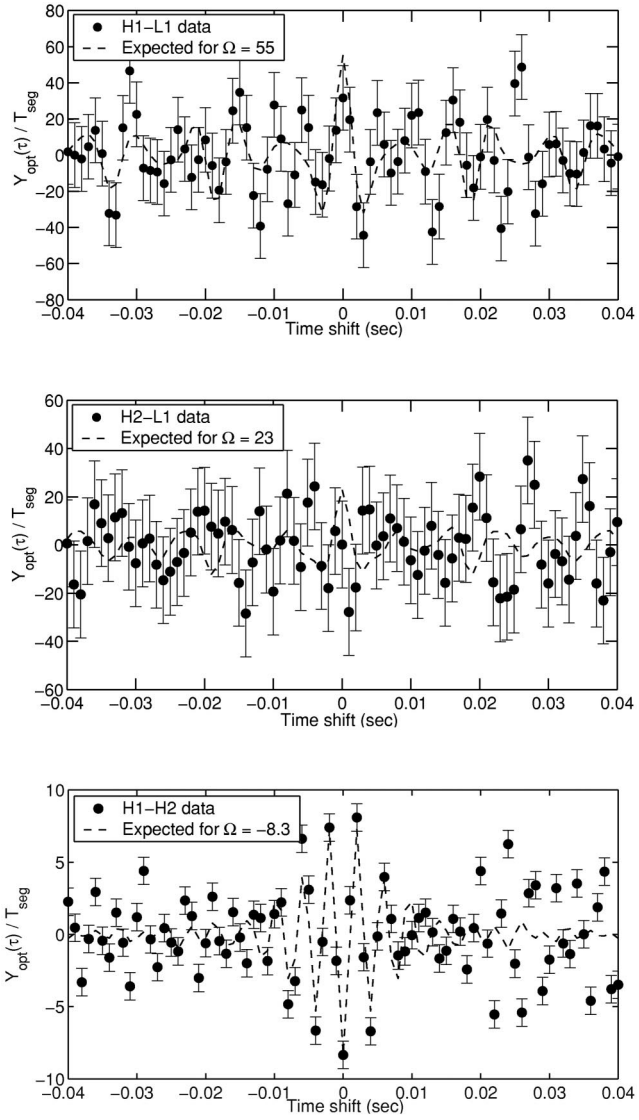

FIG. 14. Results of a time shift analysis for the three detector pairs. Plotted are the discrete inverse Fourier transforms of $\tilde{Y}_{\mathrm{opt}}[l]$. Also shown are the expected time shift curves in the presence of a stochastic background with $\Omega_{\mathrm{gw}}(f) \equiv \Omega_0 = \mathrm{const}$; for the H1-L1 and H2-L1 pairs, these are computed using the corresponding upper limit levels $\Omega_0 h_{100}^2 = 55$ and $\Omega_0 h_{100}^2 = 23$, respectively, while for H1-H2 the instrumental correlation level of -8.3 is used.

Thus, $Y(\tau)$ is simply the inverse Fourier transform of the integrand, $\tilde{Y}(f)$, of the cross-correlation statistic Y [cf. Eq. (4.3)]. The discrete frequency version of this quantity, $\tilde{Y}_{\mathrm{opt}}[\ell]$ [cf. Eq. (5.16)], is shown in Fig. 12 for each detector pair. Figure 14 shows the result of performing discrete inverse Fourier transforms on these spectra. For time shifts very small compared to the original FFT data length of 90 sec, this is equivalent to shifting the data and recalculating the point estimates.

Also shown are expected time shift curves in the presence of a significant stochastic background with $\Omega_{\mathrm{gw}}(f) \equiv \Omega_0 = \mathrm{const}$. These are obtained by taking the inverse discrete Fourier transforms of Eq. (5.28); they have an oscillating behavior reminiscent of a sinc function. For the LHO-LLO pairs, these are computed for the upper limit levels given in Table II, while for H1-H2, the expected curve is computed taking $\Omega_0 h_{100}^2$ equal to the instrumental correlation level of -8.3. For the two intersite correlations (H1-L1 and H2-L1), most of the points lie within the respective standard error levels: $\hat{\sigma}_{\Omega,\mathrm{tot}} = 18$ for H1-L1, and $\hat{\sigma}_{\Omega,\mathrm{tot}} = 18$ for H2-L1; for H1-H2, most of the points lie outside the error level, $\hat{\sigma}_{\Omega,\mathrm{tot}} = 0.95$, indicating once again that the observed H1-H2 correlation is inconsistent with the presence of a stochastic background with $\Omega_{\mathrm{gw}}(f) \equiv \Omega_0 = \mathrm{const}$.

VI. ERROR ESTIMATION

We have identified three potentially significant types of error that contribute to the total error on our estimate of $\Omega_{\mathrm{eff}} h_{100}^2$. The first is a theoretical statistical error,[13]

$$\sigma_\Omega \equiv \sigma_{Y_{\mathrm{opt}}/T_{\mathrm{seg}}} = \frac{1}{T_{\mathrm{seg}}} \frac{\sqrt{\sum_I \sigma_{Y_{IJ}}^{-4} \sigma_{Y_I}^2}}{\sum_I \sigma_{Y_{IJ}}^{-2}} \tag{6.1}$$

where the second equality follows from the definition of $\hat{\Omega}_{\mathrm{eff}} h_{100}^2$ in terms of Y_{opt} and Y_I, treating the weighting factors $\sigma_{Y_{IJ}}^{-2}$ as constants in the calculation of the theoretical variance of Y_{opt}. We estimate this error by replacing the theoretical variance $\sigma_{Y_I}^2 (= \sigma_{Y_{IJ}}^2/10)$ by its unbiased estimator $s_{Y_{IJ}}^2/10$ [cf. Eqs. (5.11),(5.12)].[14] Thus,

$$\hat{\sigma}_\Omega \equiv \frac{1}{T_{\mathrm{seg}}} \frac{1}{\sqrt{10}} \frac{\sqrt{\sum_I \sigma_{Y_{IJ}}^{-4} s_{Y_{IJ}}^2}}{\sum_I \sigma_{Y_{IJ}}^{-2}}. \tag{6.2}$$

The last two sources of error are due to unresolved time variations in the interferometers' calibration, $\sigma_{\Omega,\mathrm{cal}}$, and strain noise power spectra, $\sigma_{\Omega,\mathrm{psd}}$. As described earlier, detector power spectrum estimates are made on 900-sec data intervals, and a single response function, derived from the central 60 sec of calibration line data, is applied to each interval. Variations in both the response functions and the power spectra occur on shorter time scales, and we have estimated the systematic errors ($\hat{\sigma}_{\Omega,\mathrm{cal}}$ and $\hat{\sigma}_{\Omega,\mathrm{psd}}$) due to these variations as follows. The cross-correlation analysis is performed again using a finer time resolution for calibration and power spectrum estimation, and the results are assumed

[13]Here we are treating $\hat{\Omega}_{\mathrm{eff}} h_{100}^2$, Y_{opt}, and Y_I as *random variables* and not as their values for a particular realization of the data.

[14]This is valid provided the individual cross-correlation measurements Y_{IJ} are statistically independent of one another. This assumption was tested by computing the autocovariance function of the Y_{IJ} data sequences; for each of the three Y_{IJ} sets, the result was a delta function at zero lag, as expected for independent data samples.

TABLE IV. Sources of error in the estimate $\hat{\Omega}_{\rm eff}h_{100}^2 = Y_{\rm opt}/T_{\rm seg}$: $\hat{\sigma}_\Omega$ is the statistical error; $\hat{\sigma}_{\Omega,\rm psd}$ is the error due to unresolved time variations of the equivalent strain noise in the detectors; and $\hat{\sigma}_{\Omega,\rm cal}$ is the error due to unresolved calibration variations. The calibration uncertainty for each detector pair results from adding linearly a $\pm 10\%$ uncertainty for each detector, to allow for a worst case combination of systematic errors.

Pair	$\hat{\sigma}_\Omega$	$\hat{\sigma}_{\Omega,\rm psd}$	$\hat{\sigma}_{\Omega,\rm cal}$	$\hat{\sigma}_{\Omega,\rm tot}$	Calibration uncertainty
H1-H2	0.93	0.078	0.16	0.95	$\pm 20\%$
H1-L1	18	0.23	0.29	18	$\pm 20\%$
H2-L1	15	9.3	1.2	18	$\pm 20\%$

to be representative of the effect of variations at other time scales. Specifically, each detector pair is re-analyzed with power spectrum estimates, and corresponding optimal filters, computed for each 90-sec data segment (using the same frequency resolution as the original analysis, but approximately 1/10 the number of averages). Separately, each detector pair is also re-analyzed using the calibration line amplitudes, and resulting response functions, corresponding to each 90-sec data segment. Each analysis yields a new point estimate $\hat{\Omega}_{\rm eff}h_{100}^2$; for each re-analysis, the difference between the new point estimate and the original point estimate is used as the estimate of the systematic errors $\hat{\sigma}_{\Omega,\rm cal}$ and $\hat{\sigma}_{\Omega,\rm psd}$. The total error is then formed as:

$$\hat{\sigma}_{\Omega,\rm tot}^2 = \hat{\sigma}_\Omega^2 + \hat{\sigma}_{\Omega,\rm cal}^2 + \hat{\sigma}_{\Omega,\rm psd}^2. \tag{6.3}$$

These error estimates are shown in Table IV. Also shown in the table are values for the fractional calibration uncertainty. The significant effect here is a frequency-independent uncertainty in the response function magnitude; uncertainties in the phase response are negligible in the analysis band.

We have also considered the effect of data acquisition system timing errors on the analysis. The behavior of the cross-correlation statistic when a time offset is introduced into the analysis was shown in Fig. 14. A finer resolution plot of the time-shift curve in the presence of a significant stochastic background indicates that a $\tau = \pm 400$ μsec offset between the LHO and LLO interferometers corresponds to a 10% reduction in the estimate of our upper limit. The growth of this error is roughly quadratic in τ. Throughout the S1 run, the time-stamping of each interferometer's data was monitored, relative to GPS time. The relative timing error between H2 and L1 was approximately 40 μsec for roughly half the analyzed data set, 320 μsec for 32% of the data set, and 600 μsec for 16% of the set. The combined effect of these timing offsets is an effective reduction in the point estimate, $\hat{\Omega}_{\rm eff}h_{100}^2$, of 3.5%, a negligible effect. The H1-L1 relative timing errors were even smaller, being less than 30 μsec during the whole data set.

VII. VALIDATION: SIGNAL INJECTIONS

The analysis pipeline was validated by demonstrating the ability to detect coherent excitation of the interferometer pairs produced by simulated signals corresponding to a stationary, isotropic stochastic gravitational wave background.

A software package was developed to generate a pseudo-random time series representing this excitation. In this manner, pairs of coherent data trains of simulated stochastic signals could be generated. The amplitude of the simulated stochastic background signal was adjusted by an overall scale factor, and the behavior of the detection algorithm could be studied as a function of signal-to-noise ratio. Simulated data were either injected into the interferometer servo control system in order to directly stimulate the motion of the interferometer mirrors (*hardware injections*) or the calculated wave forms could be added in software to the interferometer data as part of the analysis pipeline (*software injections*). The former approach was used to inject a few simulated stochastic background signals of different amplitudes during interferometer calibrations at the beginning and end of the S1 run. The latter approach was used after the S1 run during the data analysis phase. Table V lists the different injections that were used to validate our procedure.

TABLE V. Summary of injected signals used to validate the analysis pipeline. Both hardware injections during the S1 run and post-S1 software injections were used. Injections were introduced into short data segments (refer to text). The signal-to-noise ratios shown correspond to integration times that are much shorter than the full S1 data set, and thus the lower signal-to-noise ratio injections were not detectable. The software and hardware injections have different signal-to-noise ratios for the same $\Omega_0 h_{100}^2$ values due to the variation in the interferometer noise power spectral densities at the different epochs when the signals were injected.

Interferometer pair	Hardware (HW) software (SW)	Magnitude of injected signal ($\Omega_0 h_{100}^2$)	Approx. SNR	Magnitude of detected signal (90% C.L., $\hat{\Omega}_0 h_{100}^2 \pm 1.65\hat{\sigma}_\Omega$)
H2-L1	HW	3906	10	3744 ± 663
H2-L1	HW	24414	17	25365 ± 2341
H2-L1	SW	16		
H2-L1	SW	100		
H2-L1	SW	625	3	891 ± 338
H2-L1	SW	3906	13	4361 ± 514
H2-L1	SW	24414	50	25124 ± 817

A. Hardware injected signals

Hardware injections required that the simulated data trains be first convolved with the appropriate instrument response functions. These pre-processed data trains were then injected digitally into the respective interferometer servo control systems.

Simulated stochastic background signals with $\Omega_{\rm gw}(f) \equiv \Omega_0 = \text{const}$ were injected simultaneously into the H2-L1 pair for two 1024 sec (17.07 min) periods shortly after the S1 run was completed. Referring to Table V, the two injections had different signal strengths, corresponding to signal-to-noise ratios of ~ 20 and ~ 10, respectively. The stronger injection produced a noticeable increase in the H2 power spectrum in the band from 40 to 600 Hz.

In principle, the stochastic gravitational wave background estimate can be derived from a single (point) measurement of the cross correlation between pairs of interferometers. However, in order to verify that the simulated signals being detected were consistent with the process being injected, time shift analyses of the data streams were performed for a number of different offsets, τ. This technique can potentially identify instrumental and environmental correlations that are not astrophysical.

For each injection, the results of the time-shifted analysis were compared with the expected time shift curves. Allowing for possible (unknown) time shifts associated with the stimulation and data acquisition processes, a two parameter χ^2 regression analysis was performed on the time shift data to determine: (i) the time offset (if any existed), (ii) the amplitude of the signal, and (iii) the uncertainties in the estimation of these parameters.

Results of this analysis for the hardware injection with signal strength $\Omega_0 h_{100}^2 = 3906$ are shown in Fig. 15. The agreement between injected simulated signal and the detected signal after end-to-end analysis with our pipeline gave us confidence that the full data analysis pipeline was working as expected.

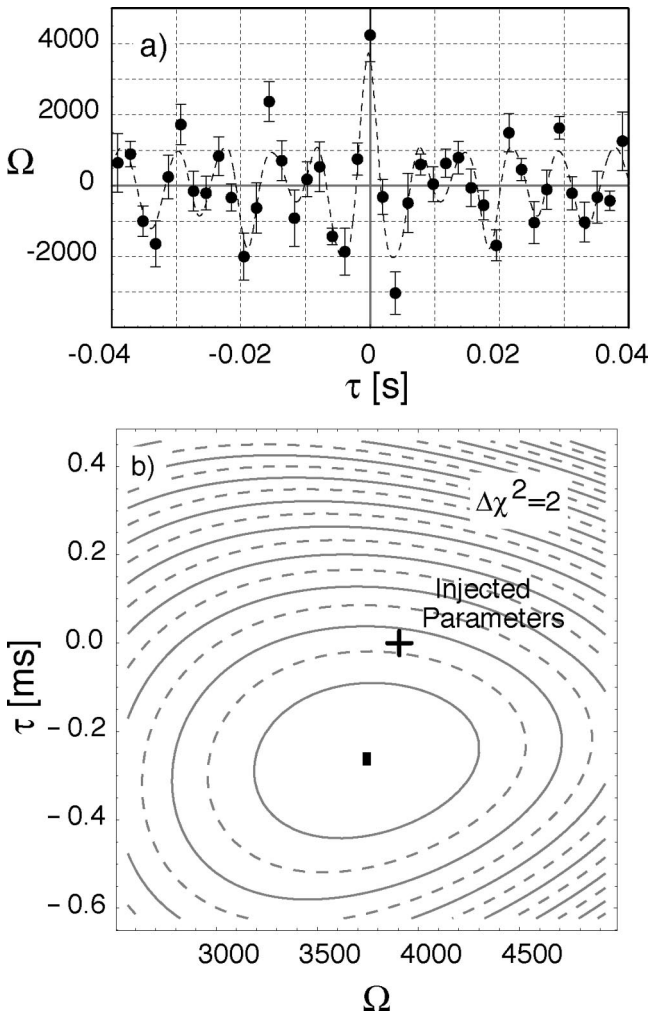

FIG. 15. Hardware injection time shift analysis for the H2-L1 interferometer pair, with signal strength $\Omega_0 h_{100}^2 = 3906$. Panel (a): Time shift dependence of the cross-correlation [refer to Eq. (5.32)]. The data are shown with $\pm 1 \hat{\sigma}_\Omega$ error bars estimated from the measured quantities [Eq. (6.1)] for each time offset. The dashed curve is the expected dependence, scaled and offset in time to provide a best fit. Panel (b): Contour plot of $\chi^2(\Omega_0, \tau)$ near the best fit. The minimum value is $\chi^2_{\rm min} = 1.8$ (for 2 degrees of freedom), and occurs at the coordinates of the black rectangle: $\{\Omega_0 h_{100}^2, \tau\} = \{3744, -270\ \mu\text{sec}\}$. The cross (+) corresponds to the injected signal, whose estimated strength has 90% confidence bounds of: $3345 \leqslant \Omega_0 h_{100}^2 \leqslant 4142$. The best fit time offset of $-270\ \mu$sec is within the observed relative data acquisition timing errors between H2 and L1 during S1.

B. Software injected signals

The same simulated signals can be written to file, and then added to the interferometer strain channels. These software simulation signals were added in after the strain data were decimated to 1024 Hz, as shown in Fig. 3. The flexibility of software injection allowed a wide range of values for $\Omega_0 h_{100}^2$ to be studied. Refer to Table V for details. This allowed us to follow the performance of the pipeline to smaller signal-to-noise ratios, until the signal could no longer be distinguished from the noise. The behavior of the deduced signal versus injected signal at a large range of signal-to-noise ratios is presented in Fig. 16.

VIII. H1-H2 CORRELATION

The significant instrumental correlation seen between the two LHO interferometers (H1 and H2) prevents us from establishing an upper limit on the gravitational wave stochastic background using what is, potentially, the most sensitive detector pair. It is thus worth examining this correlation further to understand its character. We tested the analysis pipeline for contamination from correlated spectral leakage by reanalyzing the H1-H2 data using a Hann window on the 90-sec data segments instead of the Tukey window. The result of this analysis, when scaled for the effective reduction in observation time, was—within statistical error—the same as the original Tukey-windowed analysis, discounting this hypothesis.

Some likely sources of instrumental correlations are: acoustic noise coupling to both detectors through the readout hardware (those components not located inside the vacuum

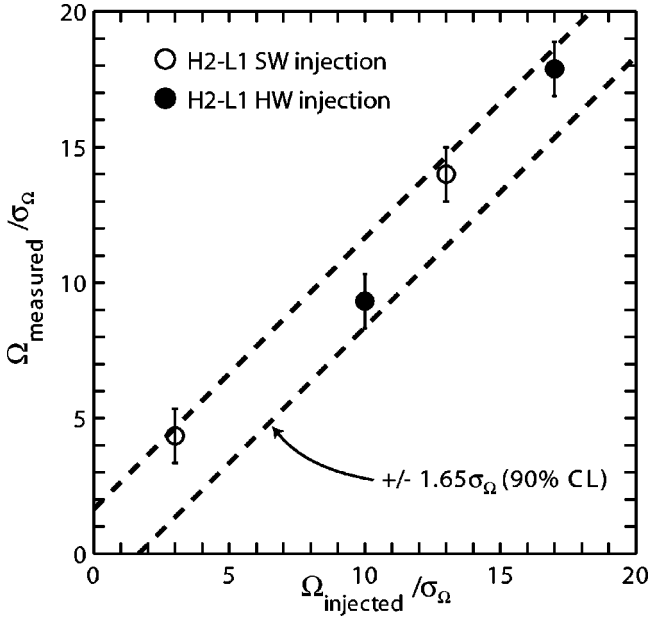

FIG. 16. H2-L1 point estimates and error bars obtained from the S1 data analysis for both hardware and software injections. Measured versus injected SNRs are shown for a number of simulations. The ordinate of each point is the result of a χ^2 analysis like the one shown in Fig. 15. The χ^2 fit also provides an estimate $\hat{\sigma}_\Omega$ of the measurement noise. The estimate is used to normalize the measured and injected values of Ω_0.

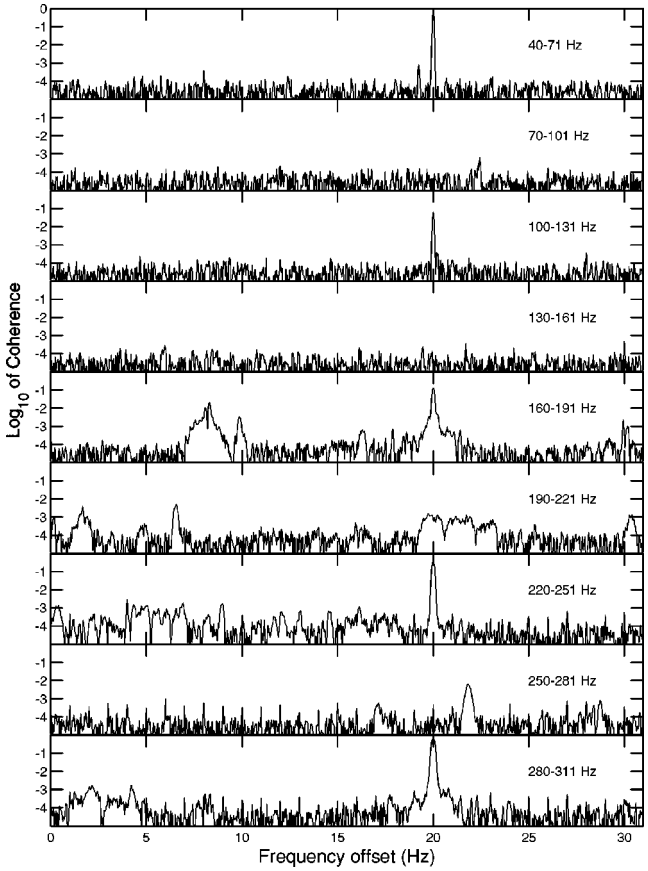

FIG. 17. Coherence between the H1 and H2 detector outputs during S1. The coherence is calculated with a frequency resolution of 0.033 Hz, and with approximately 35 000 periodogram averages; 50% overlap Hann windows were used in the Fourier transforms. In addition to the near-unity coherence at 60 Hz and harmonics, there is broadened coherence at some of these lines due to bilinear mixing of low-frequency seismic noise. There are several few-Hz wide regions of significant coherence (around 168 Hz, e.g.), and the broad region of significant coherence between 220 and 240 Hz, that are likely due to acoustic noise coupling. Also discernible are small peaks at many of the integer frequencies between 245 and 310 Hz, likely due to coupling from the GPS 1 pulse-per-second timing signals.

system); common low-frequency seismic noise that bilinearly mixes with the 60 Hz and harmonic components, to spill into the analysis band. Figure 17 shows the coherence function [Eq. (5.22)] between H1 and H2, calculated over approximately 150 h of coincident data. It shows signs of both of these types of sources.

Both of these noise sources are addressable at the instrument level. Improved electronics equipment being implemented on all detectors should substantially reduce the n60-Hz lines, and consequently the bilinearly mixed sideband components as well. Better acoustic isolation and control of acoustic sources is also being planned to reduce this noise source. It is also conceivable that signal processing techniques, such as those described in Refs. [41,42], could be used to remove correlated noise, induced by measurable environmental disturbances, from the data.

IX. CONCLUSIONS AND FUTURE PLANS

In summary, we have analyzed the first LIGO science data to set an improved, direct observational upper limit on a stochastic background of gravitational waves. Our 90% confidence upper limit on a stochastic background, having a constant energy density per logarithmic frequency interval, is $\Omega_0 h_{100}^2 \leqslant 23$ in the frequency band 40–314 Hz. This is a roughly 10^4 times improvement over the previous, broadband interferometric detector measurement.

We described in detail the data analysis pipeline, and tests of the pipeline using hardware and software injected signals. We intend to use this pipeline on future LIGO science data to set upper limits on $\Omega_0 h_{100}^2$ at levels which are orders of magnitude below unity. Two possible additions to the treatment presented here are being considered for future analyses: a method for combining upper limits from H1-L1 and H2-L1 that takes into account the potential H1-H2 instrumental correlations; a Bayesian statistical analysis for converting the point estimate into an upper limit on $\Omega_0 h_{100}^2$. Eventually, with both 4-km interferometers (H1 and L1) operating at the design sensitivity level shown in Fig. 1, we expect to be able to set an upper limit using 1 year of data from this detector pair at a level $\Omega_0 h_{100}^2 \leqslant 1 \times 10^{-6}$ in the 40–314-Hz band. This would improve on the limit from big-bang nucleosynthesis (see Table I). The two interferometers at LHO (H1 and H2) could potentially provide a lower upper limit, but given our present level of correlated instrumental noise

($|\hat{\Omega}_{\rm inst}h_{100}^2| \sim 10$), we first need to reduce the correlated noise in each detector by a factor of $\sim 10^4$. We also intend on searching for different power laws than the f^{-3} power spectrum corresponding to the constant $\Omega_{\rm gw}$ model. Finally, we anticipate cross correlating L1 with the ALLEGRO resonant bar detector (located nearby LLO in Baton Rouge, LA) for a higher frequency search. With this pair performing at design sensitivity, an upper limit of order $\Omega_0 h_{100}^2 \leqslant 0.01$ could be set around 900 Hz, using 1 year of coincident data.

ACKNOWLEDGMENTS

The authors gratefully acknowledge the support of the United States National Science Foundation for the construction and operation of the LIGO Laboratory and the Particle Physics and Astronomy Research Council of the United Kingdom, the Max-Planck-Society and the State of Niedersachsen/Germany for support of the construction and operation of the GEO600 detector. The authors also gratefully acknowledge the support of the research by these agencies and by the Australian Research Council, the Natural Sciences and Engineering Research Council of Canada, the Council of Scientific and Industrial Research of India, the Department of Science and Technology of India, the Spanish Ministerio de Ciencia y Tecnologia, the John Simon Guggenheim Foundation, the David and Lucile Packard Foundation, the Research Corporation, and the Alfred P. Sloan Foundation. This paper has been assigned LIGO Document Number LIGO-P030009-H-Z.

APPENDIX: LIST OF SYMBOLS

The following is a list of symbols that appear in the paper, along with their descriptions and equation numbers (if applicable) or sections in which they were defined.

Symbol	Description	Eq. no./section
$\Omega_{\rm gw}(f)$	Energy density in gravitational waves per logarithmic frequency interval in units of the closure energy density ρ_c	(3.1)
$\rho_c, \rho_{\rm gw}$	Critical energy density needed to close the universe, and total energy density in gravitational waves	III A
h_{100}, H_0, H_{100}	h_{100} is the Hubble constant, H_0, in units of $H_{100} \equiv 100$ km/sec/Mpc	(3.2),(3.3)
$h_{ab}(t), h(t)$	Perturbations of the space-time metric, and the corresponding gravitational wave strain in a detector	(3.5)
$\vec{x}_0, \hat{X}^a, \hat{Y}^a$	Position vector of an interferometer vertex, and unit vectors pointing in the directions of the arms of an interferometer	(III A)
$S_{\rm gw}(f)$	Power spectrum of the gravitational wave strain $h(t)$	(3.6)
$s_i(t), \tilde{s}_i(f)$	Equivalent strain output of the ith detector	(4.1)
$h_i(t), \tilde{h}_i(f)$	Gravitational wave strain in the ith detector	(4.1)
$n_i(t), \tilde{n}_i(f)$	Equivalent strain noise in the ith detector	(4.1)
$r_i(t), r_i[k]$	Raw (i.e., uncalibrated) output of the ith detector for continuous and discrete time	(5.1)
$\tilde{R}_i(f)$, $\tilde{R}_{iI}[\ell]$	Response function for the ith detector, and the discrete frequency response function for interval I	V A
t_k, f_ℓ	Discrete time and discrete frequency values	V A
$\delta t, \delta f$	Sampling period of the time-series data (1/1024 sec after down sampling), and bin spacing (0.25 Hz) of the discrete power spectra, optimal filter, ...	V A
Δf	General frequency resolution of discrete Fourier transformed data	V C
N	Number of discrete-time data points in one segment of data	V A
$r_{iIJ}[k], g_{iIJ}[k], \tilde{g}_{iJK}[q]$	Raw detector output for the Jth segment in interval I evaluated at discrete time t_k, and the corresponding windowed and zero-padded time series and discrete Fourier transform	(5.2)
$\mathcal{G}_{IJ}[\ell]$	Cross spectrum of the windowed and zero-padded raw time series, binned to match the frequency resolution of the optimal filter $\tilde{Q}_I[\ell]$	(5.4)
$w_i[k]$	Window function for the ith detector	V A
n_b	Number of frequency values binned together to match the frequency resolution of the optimal filter $\tilde{Q}_I[\ell]$	V A
$\ell_{\rm min}, \ell_{\rm max}$	Indices corresponding to the minimum and maximum frequencies used in the calculation of the cross correlation Y_{IJ}	V A
$\delta_T(f)$	Finite-time approximation to the Dirac delta function $\delta(f)$	(4.4)

$T, T_{\rm seg}, T_{\rm int}$	General observation time, and durations of an individual data segment and interval (90 sec, 900 sec)	V A
Y	General cross correlation of two detectors	(4.2)
$Q(t), \tilde{Q}(f)$	Optimal filter for the cross correlation Y	(4.8)
$\mu_Y, \sigma_Y^2, \rho_Y$	Theoretical mean, variance, and signal-to-noise ratio of the cross correlation Y	(4.5),(4.6)
$\langle \rho_Y \rangle$	Expected value of the signal-to-noise ratio of the cross correlation Y	(4.11)
Y_{IJ}, Y_I	Cross correlation for the Jth segment in interval I, and average of the Y_{IJ}	(5.5),(5.11)
$Y_{\rm opt}$	Weighted average of the Y_I	(5.13)
x_{IJ}	Cross-correlation values Y_{IJ} with mean removed and normalized by the theoretical variances	V D
$\tilde{Y}_{IJ}[\ell], \tilde{Y}_I[\ell], \tilde{Y}_{\rm opt}[\ell]$	Summands of Y_{IJ}, Y_I, $Y_{\rm opt}$	(5.14),(5.15),(5.16)
$\tilde{Q}_I[\ell]$	Optimal filter for the cross correlation Y_{IJ}	(5.6)
$\gamma(f), \gamma[\ell]$	Overlap reduction function evaluated at frequency f, and discrete frequency f_ℓ	IV, V A
$\gamma_{\rm rms}, \Delta_{\rm BW}$	Root-mean-square value of the overlap reduction function over the corresponding frequency bandwidth $\Delta_{\rm BW}$	IV
$P_i(f), P_{iI}[\ell]$	Power spectrum of the strain noise in the ith detector, and the discrete frequency strain noise power spectrum estimate for interval I	IV, V A
$\mathcal{N}$, $\mathcal{N}_I$	Normalization factors for the optimal filter $\tilde{Q}$, $\tilde{Q}_I$	(4.9),(5.7)
$\overline{w_1 w_2}$, $\overline{w_1^2 w_2^2}$	Overall multiplicative factors introduced by windowing	(5.9),(5.10)
$\sigma^2_{Y_{IJ}}, s^2_{Y_{IJ}}$	Theoretical and estimated variance of the cross correlation Y_{IJ}	(5.8),(5.12)
$\sigma^2_{Y_I}, \sigma^2_{Y_{\rm opt}}$	Theoretical variance of Y_I and $Y_{\rm opt}$	VI
$\mu_{\tilde{Y}_{\rm opt}}[\ell], \sigma^2_{\tilde{Y}_{\rm opt}}[\ell]$	Theoretical mean and variance of $\tilde{Y}_{\rm opt}[\ell]$	(5.28),(5.29)
$P_{12}(f)$	Cross-power spectrum of the strain noise between two detectors	V C
$\Gamma_{12}(f)$	Coherence function between two detectors	(5.22)
$N_{\rm avg}, \sigma_\Gamma$	Number of averages used in the measurement of the coherence, and the corresponding statistical uncertainity in the measurement	V C
$\Omega_0, \hat{\Omega}_0$	Actual and estimated values of an (assumed) constant value of $\Omega_{\rm gw}(f)$ due to gravitational waves	III A, V A
$\Omega_{\rm inst}, \hat{\Omega}_{\rm inst}$	Actual and estimated values of the instrumental contribution to the measured cross correlation	V D
$\Omega_{\rm eff}, \hat{\Omega}_{\rm eff}$	Actual and estimated values of an effective Ω due to instrumental and gravitational wave effects	(5.24)
$\sigma^2_\Omega, \hat{\sigma}^2_\Omega$	Actual and estimated variances of $\hat{\Omega}_{\rm eff}$ due to statistical variations in $Y_{\rm opt}$	(6.1),(6.2)
$\sigma^2_{\Omega,\rm cal}, \hat{\sigma}^2_{\Omega,\rm cal}$	Actual and estimated variances of $\hat{\Omega}_{\rm eff}$ due to variations in the instrument calibration	VI
$\sigma^2_{\Omega,\rm psd}, \hat{\sigma}^2_{\Omega,\rm psd}$	Actual and estimated variances of $\hat{\Omega}_{\rm eff}$ due to variations in the noise power spectra	VI
$\hat{\sigma}^2_{\Omega,\rm tot}$	Estimated variance of $\hat{\Omega}_{\rm eff}$ due to combined statistical, calibration, and power spectra variations	(6.3)
$\chi^2(\Omega_0)$	Chi-squared statistic to compare $\tilde{Y}_{\rm opt}[\ell]$ to its expected value for a stochastic background with $\Omega_{\rm gw}(f) \equiv \Omega_0$	(5.27)
$\chi^2_{\rm min}$	Minimum chi-squared value per degree of freedom	V E
$Y(\tau), \tilde{Y}(f)$	Cross correlation statistic as a function of time shift τ, and its Fourier transform	(5.32),(5.33)

[1] B. Barish and R. Weiss, Phys. Today **52** (10), 44 (1999); http://www.ligo.caltech.edu/

[2] B. Willke *et al.*, Class. Quantum Grav. **19**, 1377 (2002); http://www.geo600.uni-hannover.de/

[3] B. Caron *et al.*, Nucl. Phys. B (Proc. Suppl.) **54**, 167 (1997); http://www.virgo.infn.it/

[4] K. Tsubono, in *1st Edoardo Amaldi Conf. on Gravitational Wave Experiments*, edited by E. Coccia, G. Pizzella, and F. Ronga (World Scientific, Singapore, 1995), p. 112.

[5] R. Savage, P. King, and S. Seel, Laser Phys. **8**, 679 (1998).

[6] J. Giaime, P. Saha, D. Shoemaker, and L. Sievers, Rev. Sci. Instrum. **67**, 208 (1996).

[7] J.A. Giaime, E.J. Daw, M. Weitz, R. Adhikari, P. Fritschel, R. Abbott, R. Bork, and J. Heefner, Rev. Sci. Instrum. **74**, 218 (2003).

[8] P. Fritschel, R. Bork, G. González, N. Mavalvala, D. Ouimette, H. Rong, D. Sigg, and M. Zucker, Appl. Opt. **40**, 4988 (2001).

[9] P. Fritschel, N. Mavalvala, D. Shoemaker, D. Sigg, M. Zucker, and G. González, Appl. Opt. **37**, 6734 (1998).

[10] R. Adhikari, G. González, M. Landry, and B. O'Reilly, Class.

Quantum Grav. **20**, S903 (2003).
[11] LIGO Scientific Collaboration, Nucl. Instrum. Methods Phys. Res. A **517**, 154 (2004).
[12] B. Allen, in *Proceedings of the Les Houches School on Astrophysical Sources of Gravitational Waves, Les Houches, 1995*, edited by J. A. Marck and J. P. Lasota (Cambridge University Press, Cambridge, England, 1996), p. 373.
[13] M. Maggiore, Phys. Rep. **331**, 283 (2000).
[14] W. Freedman *et al.*, Astrophys. J. **553**, 47 (2001).
[15] B.K. Gibson and C.B. Brook, in *New Cosmological Data and the Values of the Fundamental Parameters*, edited by A. N. Lasenby and A. Wilkinson (Astronomical Society of the Pacific, San Francisco, in press), astro-ph/0011567.
[16] C.L. Bennett *et al.*, Astrophys. J., Supp. Ser. **148**, 1 (2003).
[17] C. W. Misner, K. S. Thorne, and J. A. Wheeler, *Gravitation* (Freeman, San Francisco, 1973).
[18] B. Allen and J.D. Romano, Phys. Rev. D **59**, 102001 (1999).
[19] R.R. Caldwell, R.A. Battye, and E.P.S. Shellard, Phys. Rev. D **54**, 7146 (1996).
[20] D.M. Coward, R.R. Burman, and D.G. Blair, Mon. Not. R. Astron. Soc. **324**, 1015 (2001).
[21] V. Ferrari, S. Matarrese, and R. Schneider, Mon. Not. R. Astron. Soc. **303**, 247 (1999).
[22] B. Allen and A.C. Ottewill, Phys. Rev. D **56**, 545 (1997).
[23] S. Drasco and É.É. Flanagan, Phys. Rev. D **67**, 082003 (2003).
[24] M.S. Turner, Phys. Rev. D **55**, R435 (1997).
[25] M.P. McHugh, G. Zalamansky, F. Vernotte, and E. Lantz, Phys. Rev. D **54**, 5993 (1996).
[26] E. W. Kolb and M. Turner, *The Early Universe* (Addison-Wesley, Reading, MA, 1990).
[27] J. Hough, J.R. Pugh, R. Bland, and R.W. Drever, Nature (London) **254**, 498 (1975).
[28] K. Compton, D. Nicholson, and B. F. Schutz, in *Proceedings of the Seventh Marcel Grossman Meeting on General Relativity* (World Scientific, Singapore, 1994), p. 1078.
[29] P. Astone *et al.*, Phys. Lett. B **385**, 421 (1996).
[30] P. Astone *et al.*, Astron. Astrophys. **343**, 19 (1999).
[31] P. Astone *et al.*, Astron. Astrophys. **351**, 811 (1999).
[32] P. Astone, V. Ferrari, M. Maggiore, and J.D. Romano, Int. J. Mod. Phys. D **9**, 361 (2000).
[33] P.F. Michelson, Mon. Not. R. Astron. Soc. **227**, 933 (1987).
[34] N. Christensen, Phys. Rev. D **46**, 5250 (1992).
[35] É.É. Flanagan, Phys. Rev. D **48**, 2389 (1993).
[36] The large-scale computing was carried out on Linux clusters at Caltech and the University of Wisconsin–Milwaukee (the UWM Medusa cluster, http://www.lsc-group.phys.uwm.edu/beowulf/medusa), partially supported by the GriPhyN (http://www.griphyn.org) and iVDGL (http://www.ivdgl.org) projects.
[37] W. H. Press, B. P. Flannery, S. A. Teukolsky, and W. T. Vetterling, in *Numerical Recipes in C* (Cambridge University Press, Cambridge, England, 1992), second edition.
[38] ''Cross-correlation of windowed, discretely-sampled data,'' J. T. Whelan, LIGO Technical Document LIGO-T040125-00-Z.
[39] J. G. Proakis and D. G. Manolakis, in *Digital Signal Processing*: *Principles*, *Algorithms*, *and Applications* (Prentice-Hall, Upper Saddle River, NJ, 1996), third edition, p. 624.
[40] J. S. Bendat and A. G. Piersol, in *Random Data*: *Analysis and Measurement Procedures* (Wiley-Interscience, New York, 2000), third edition, p. 147.
[41] B. Allen, W. Hua, and A. Ottewill, gr-qc/9909083.
[42] A.C. Searle, S.M. Scott, and D.E. McClelland, Class. Quantun Grav. **20**, S721 (2003).